

Chapter 5

evolution of crustal magnetic field in an accreting neutron star

5.1 introduction

It has been discussed in chapter [3] that observations suggest a connection between the low magnetic field of binary and millisecond pulsars and their being processed in binary systems, indicating accretion-induced field decay in such systems. A possible mechanism for such decay is understood to be the rapid ohmic dissipation of the currents in the accretion heated crust (see section [3.3] for details). In this work we explore models that primarily depend on this microscopic process of ohmic decay for a permanent reduction in the observed field strength, and also on the large scale material movement for the final stabilization of the field. Here we shall investigate a model based on the assumption that the current loops responsible for the magnetic field are initially confined entirely within the crust. This situation is likely to be the result of a generation of the field due to thermo-magnetic instabilities after the birth of the star (see section [3.2] for details). If the initial field resides mainly in the superconducting core then our scenario would apply only after most of this flux has been expelled into the crust, a situation which will be treated in chapter [7].

The crustal field undergoes ohmic diffusion due to the finite electrical conductivity of the crustal lattice, but the time-scale of such decay is very long under ordinary conditions (Sang & Chanmugam 1987; Urpin & Muslimov 1992). The situation changes significantly when accretion is turned on. The heating of the crust reduces the electrical conductivity by several orders of magnitude, thereby reducing the ohmic decay time-scale. As the mass increases, a neutron star becomes more and more compact and the mass of the crust actually decreases by a small amount (see section [2.2]). So the newly accreted material forms the crust and the original crustal material gets continu-

ally assimilated into the superconducting core beneath. The original current carrying layers are thus pushed into deeper and more dense regions as accretion proceeds. This compression results in a decrease of the effective length scale of the current loops which makes a fast dissipation possible (Konar, Bhattacharya & Urpin 1995). But the higher conductivity of the denser regions would progressively slow down the decay winning over the effect of a decrease in the length scale, till the current loops are completely inside the superconducting region where any further decay is prevented.

The organization of the chapter is as follows. In section [5.2] we discuss the physics of the field reduction in an accreting neutron star, computational details are discussed in section [5.3]. Finally in section [5.4] we present our results and draw the conclusions in section [5.5].

5.2 physics of the mechanism

The evolution of the crustal field as a result of ohmic diffusion and material motion has been discussed by a number of authors (Wendell, van Horn & Sargent 1987; Sang & Chanmugam 1987; Geppert & Urpin 1994) and essentially concerns the solution of the following equation (Jackson, 1975)

$$\frac{\partial \vec{B}}{\partial t} = \vec{\nabla} \times (\vec{V} \times \vec{B}) - \frac{c^2}{4\pi} \vec{\nabla} \times \left(\frac{1}{\sigma} \times \vec{\nabla} \times \vec{B} \right) \quad (5.1)$$

where \vec{V} is the velocity of material movement and σ is the electrical conductivity of the medium. As in previous studies we solve this equation by introducing the vector potential \vec{A} , such that

$$\vec{B} = \nabla \times \vec{A} \quad (5.2)$$

where, $\vec{A} = (0, 0, A_\phi)$. This choice of the vector potential ensures a poloidal geometry for \vec{B} . In particular, we choose

$$A_\phi = \frac{g(r, t) \sin \theta}{r}, \quad g(r, t) \text{ is the Stokes' function,} \quad (5.3)$$

(r, θ, ϕ) being the spherical polar co-ordinates. Here we work in the lowest order of multipole, obtaining the following dipolar form of the magnetic field :

$$\begin{aligned} \vec{B}(r, \theta) &= \vec{\nabla} \times \left(\frac{g(r, t) \sin \theta}{r} \hat{\phi} \right) \\ &= \frac{2 \cos \theta g(r, t) \hat{r}}{r^2} - \frac{\sin \theta}{r} \frac{\partial g(r, t)}{\partial r} \hat{\theta}. \end{aligned} \quad (5.4)$$

The magnitude of the field is given by,

$$B(r, \theta) = \left[\frac{4 \cos^2 \theta g^2(r, t)}{r^4} + \frac{\sin^2 \theta}{r^2} \left(\frac{\partial g(r, t)}{\partial r} \right)^2 \right]^{1/2} \quad (5.5)$$

Therefore, at the pole ($\theta = 0$, $r = R$) the magnitude is

$$B(R, 0) = \frac{2g(R, t)}{R^2}, \quad (5.6)$$

which is simply proportional to the value of the Stokes' function there. We shall use this fact to obtain the evolution of the surface field with time.

The underlying current distribution corresponding to the above field is obtained by using Maxwell's equation :

$$\begin{aligned} \vec{j} &= \frac{c}{4\pi} \nabla \times \vec{B} \\ &= -\frac{c}{4\pi} \frac{\sin \theta}{r} \left[\frac{\partial^2 g(r, t)}{\partial r^2} - \frac{2g(r, t)}{r^2} \right] \hat{\phi}. \end{aligned} \quad (5.7)$$

5.2.1 ohmic diffusion

In order to understand the ohmic dissipation of the field strength, let us consider equation [5.1] without the first term on the right hand side. The first term corresponds to the convective transport, which we shall discuss later. Without this term equation [5.1] takes the following form,

$$\frac{\partial \vec{B}}{\partial t} = -\frac{c^2}{4\pi} \vec{\nabla} \times \left(\frac{1}{\sigma} \times \vec{\nabla} \times \vec{B} \right). \quad (5.8)$$

For the moment, let us consider the conductivity to be a constant, without any dependence on space. Then, the above equation takes the form of a pure diffusion equation (by virtue of the divergence-free condition for the magnetic fields), given by

$$\frac{\partial \vec{B}}{\partial t} = \frac{c^2}{4\pi\sigma} \nabla^2 \vec{B}. \quad (5.9)$$

The diffusion constant for the above equation is $\frac{c^2}{4\pi\sigma}$. One can define a time-scale characteristic of the diffusion process :

$$\tau_{\text{diff}} = \frac{4\pi\sigma L^2}{c^2}, \quad (5.10)$$

where L is the length-scale associated with the underlying current distribution supporting the field.

It is clear from equation [5.10] that the rate of ohmic diffusion is determined mainly by the electrical conductivity of the crust which is a steeply increasing function of density (see figures in section [2.4]). As density in the crust spans eight orders of magnitude with a very large radial gradient the conductivity changes sharply as a function of depth from the neutron star surface. Thus the deeper the location of the current distribution, the slower is the decay. We have discussed, in detail, the effects of temperature and that of impurity concentration on the conductivity in section [2.4], also about the change in the thermal behaviour in presence of accretion in a neutron star in section [2.3]. The increase in temperature of an accretion-heated crust lowers the conductivity and therefore the time-scale for the diffusion decreases. In other words, the transfer of the energy of the systematic motion of the charge carriers (the electrons) within the current loops into the random kinetic energy of the electrons proceed at a faster rate at a higher temperature. For the models we are considering now, it has been assumed in the literature that the impurity strength Q lies in the range 0.01 - 0.1. The effect of impurities is most important at lower temperatures and higher densities (see figures [2.21] and [2.22]). Therefore the field evolution does not show any significant dependence on impurity strength for this range of Q in an accretion-heated crust. We therefore restrict our computations to the $Q = 0.0$ case. However, the impurity strength will still play an important role in field decay during the pre-accretion phase when the crustal temperatures can be quite low.

5.2.2 accretion and material transport

In a neutron star, for a given equation of state, the mass of the crust is uniquely determined by the total mass of the star (see section [2.2]). And this crustal mass remains effectively constant for the accreted masses of the order of $0.1 M_{\odot}$ with a slight decrease as the total mass increases (see figures [2.14], [2.15] and [2.16]). For example, for the equation of state that we have used (see section [2.1] for details) the accretion of $0.1 M_{\odot}$ on the star causes a change in the crustal mass of only $0.004 M_{\odot}$. As a result, accretion causes continuous assimilation of material from the bottom of the crust into the core. At the same time the upper layers of the original crust are pushed to deeper and denser regions, leading to extreme squeeze of this material. This also causes the current distribution embedded in this material to be sharpened, reducing the effective length scale of the system.

The change in the crustal mass and the crustal density profile is negligible for the

amount of mass accretion we consider. We therefore take the mass flux to be the same throughout the crust, equal to its value at the surface. Assuming the mass flow to be spherically symmetric in the crustal layers of interest, one obtains the following condition for the equality of mass flux at all densities within the crust,

$$\begin{aligned} \dot{M} dt &= 4\pi r^2 \rho(r) dr, \\ \Rightarrow V(r) &= \frac{\dot{M}}{4\pi r^2 \rho(r)}, \end{aligned} \quad (5.11)$$

where \dot{M} is the rate of mass accretion and $\rho(r)$ is the density as a function of radius r . The above equation defines $V(r)$ - the velocity of radial material flow at a given radius in the crust. It should be noted here that the material flow is radially inwards, hence writing the flow velocity in its full vectorial form we have,

$$\vec{V}(r) = -\frac{\dot{M}}{4\pi r^2 \rho(r)} \hat{r}. \quad (5.12)$$

The result of accretion on the magnetic field evolution therefore manifests itself as a combination of three effects: transport of the current distribution to regions of higher density and hence higher conductivity, reduction of conductivity due to heating and change in the effective length scale of the current distribution (see Bhattacharya 1995a for a detailed discussion). We find that the overall effect turns out to be a rapid initial decay followed by a leveling off when an amount of mass equivalent to about 10% of the original crust has been accreted. By this time the current loops reach the regions of very high density and consequently of extremely large conductivity where the diffusion time-scales are much too long. As further accretion proceeds the original crust is assimilated into the superconducting interior freezing the currents there. Following Baym, Pethick & Pines (1969) we assume that the newly formed superconducting material retains the magnetic flux through it in the form of Abrikosov fluxoids rather than expelling it through the Meissner effect.

5.2.3 the field evolution equation

We use the form of $B(r, \theta, \phi)$ given by equation [5.4] and the form of \vec{V} given by equation [5.12] to cast equation [5.1] in terms of the Stokes' function.

1. The left hand side -

$$\begin{aligned} \frac{\partial \vec{B}}{\partial t} &= \frac{\mathbf{a} \mathbf{v} \times \vec{A}}{\partial t} \\ &= \mathbf{v} \times \frac{\partial}{\partial t} \left[\frac{g(r, \theta) \sin \theta}{r} \right] \hat{\phi}. \end{aligned} \quad (5.13)$$

2. The first term in the right hand side -

$$\begin{aligned} \mathbf{V} \times (\vec{V} \times \vec{B}) &= \mathbf{V} \times \left[(-V(r) \hat{r}) \times \left(\frac{2 \cos \theta}{r^2} g(r, t) \hat{r} - \frac{\sin \theta}{r} \frac{\partial g(r, t)}{\partial r} \hat{\theta} \right) \right] \\ &= \nabla \times \left[\frac{\sin \theta}{r} V(r) \frac{dg(r, t)}{dr} \right] \hat{\phi}. \end{aligned} \quad (5.14)$$

3. The second term in the right hand side -

$$\begin{aligned} \nabla \times \left[\frac{1}{\sigma} \nabla \times \vec{B} \right] &= \nabla \times \left[\frac{1}{\sigma} \nabla \times \left(\frac{2 \cos \theta}{r^2} g(r, t) \hat{r} - \frac{\sin \theta}{r} \frac{\partial g(r, t)}{\partial r} \hat{\theta} \right) \right] \\ &= \nabla \times \left[-\frac{1}{\sigma} \frac{\sin \theta}{r} \left(\frac{\partial^2 g(r, t)}{\partial r^2} - \frac{2g(r, t)}{r^2} \right) \hat{\phi} \right]. \end{aligned} \quad (5.15)$$

Incorporation of the expressions [5.13], [5.14] and [5.15] in the equation [5.1] then leads

$$\frac{\partial g(r, t)}{\partial t} = V(r) \frac{\partial g(r, t)}{\partial r} + \frac{c^2}{4\pi\sigma} \left(\frac{\partial^2 g(r, t)}{\partial r^2} - \frac{2g(r, t)}{r^2} \right). \quad (5.16)$$

The results of this chapter will be based on numerical solutions of the equation [5.16].

5.3 computations

The aim of our computations is to solve equation [5.16] to obtain $g(r, t)$ using the following boundary conditions valid for all times (see, e.g., Geppert & Urpin 1994):

$$\frac{\partial g(r, t)}{\partial r} \Big|_{r=R} + \frac{g(R, t)}{R} = 0, \quad (5.17)$$

$$g(r_{\text{co}}, t) = 0 \quad (5.18)$$

where R is radius of the star and r_{co} is that radius to which the original boundary between the core and the crust is pushed to, due to accretion, at any point of time. The first condition matches the interior field to an external dipole configuration. The second condition indicates that as accretion proceeds along with the crustal material the frozen-in flux moves inside the core, but the field can not diffuse through the original crust-core boundary. To simulate an effectively infinite conductivity in the region between the bottom of the crust and the original boundary between the crust and the core, we set a $\sim 10^{50} \text{s}^{-1}$ in this region. As mentioned before, we take into account the combined effects of accretion driven material motion and ohmic diffusion. We construct the density profile of a neutron star as described in section [2.2] for an assumed mass of $1.4 M_{\odot}$. This star has a total crustal mass of $0.044 M_{\odot}$ and we restrict our evolutionary calculations to a maximum net accretion of this additional amount on the star, because an accretion of that amount of material pushes the original crust completely within

the core. The change in the crustal density profile resulting from this additional mass is negligible. Hence we work with an invariant crustal density profile throughout our calculation.

We assume that the matter settling onto the star does so uniformly across the entire surface. This allows us to use the expression of $V(r)$ as in equation [5.11]. When the surface magnetic field is strong this is a poor approximation very close to the surface (see the discussion about anisotropic material transport in section [4.2] However in deeper layers ($\rho \gtrsim 10^{10} \text{ g cm}^{-3}$) which we are mainly concerned with, the material motion is essentially dictated by the added weight and is going to be more or less isotropic.

We further assume that the incoming matter fully threads the existing magnetic field before settling onto the surface. In other words we allow for no reduction of the external magnetic field arising out of diamagnetic screening by the incoming material. We adopt this scheme to ensure that the effects under investigation here, namely diffusion and convection, do not get masked by other effects such as screening. In the light of the results obtained in the previous chapter regarding diamagnetic screening, we are quite justified in making such an assumption.

We assume that during the phase of mass accretion the temperature in the crust is uniform and remains constant in time. This ignores an initial short phase in which both the rate of accretion and the temperature of the crust show time evolution. The rate of accretion stabilizes in a few thousand years (Savonije 1978) and the temperature within 10^5 yrs (Miralda-Escudé et al. 1990). Computations by Urpin & Geppert (1996) show that the decay during this initial phase is insignificant. The temperature that the crust will finally attain in the steady phase has been computed by Fujimoto et al. (1984), Miralda-Escudé et al. (1990) and Zdunik et al. (1992). However, these computations are restricted to limited range of mass accretion and also do not yield the same crustal temperature under similar conditions. The results obtained by Zdunik et al. (1992) for the crustal temperatures for a given accretion rate in the range $10^{-15} \text{ M}_{\odot} \text{ yr}^{-1} \lesssim \dot{M} \lesssim 2 \times 10^{-10} \text{ M}_{\odot} \text{ yr}^{-1}$ could be fitted to the equation [2.13]. But extrapolation of this fit to higher rates of accretion gives extremely high temperatures which may not be sustainable for any reasonable period due to rapid cooling by neutrinos at those temperatures. We have therefore restricted our computations to a maximum accretion rate of $10^{-9} \text{ M}_{\odot} \text{ yr}^{-1}$ and for \dot{M} in the range $10^{-10} - 10^{-9} \text{ M}_{\odot} \text{ yr}^{-1}$, we have explored a range of constant crustal temperatures between 10^8 and $10^{8.75}$ K.

In a series of papers Geppert & Urpin (1994), Urpin & Geppert (1995, 1996) and Geppert, Urpin & Kononov (1996) have considered evolution of crustal magnetic field for accretion rates in the range $10^{-15} - 10^{-9} M_{\odot} \text{ yr}^{-1}$. In this work we too consider accretion rates covering much of the above range. The difference between our computations and those in the above papers lies in the range of total mass accretion and the treatment of the inner boundary condition. Our computations proceed to a maximum net accretion of $\sim 4 \times 10^{-2} M_{\odot}$ whereas the computations by other authors are restricted to that of the order of $10^{-3} M_{\odot}$. Our choice of the range of accretion rates also facilitates the comparison of our results with those available in the literature, over the range of overlap in the net mass accreted. At accreted masses $\gtrsim 10^{-3} M_{\odot}$, the inward convection of currents into the core becomes significant. As computations by previous authors do not allow for this possibility, our results begin to diverge from theirs for high values of accreted mass.

5.3.1 numerical scheme

We solve the equation [5.16] in terms of fractional radius, x , instead of the radius. Re-writing this equation in terms of the fractional radius, we obtain,

$$\frac{\partial g(x, t)}{\partial t} = V(x) \frac{\partial g(x, t)}{\partial x} + S(x, t) \left(\frac{\partial^2 g(x, t)}{\partial x^2} - \frac{2g(x, t)}{x^2} \right), \quad (5.19)$$

where,

$$V(x) = V(r)/R, \quad (5.20)$$

$$S(x, t) = \frac{c^2}{4\pi\sigma(r, t)R^2}. \quad (5.21)$$

To solve the above equation we use a modified Crank-Nicholson scheme. Since the conductivity is a function of density and hence of radius, it has been necessary to incorporate the space dependence of conductivity in the standard Crank-Nicholson scheme of differencing. In addition we also allow for a pre-accretion phase where the neutron star undergoes normal cooling. This introduces a time-dependence in the temperature and hence in the diffusion-constant as well. The overall effect is to consider an explicit space-time dependence of the function $S(x)$ which is a pre-factor to the diffusion term. We introduce the convection term into the computation through upwind differencing and operator splitting of the full differential equation (Press et al. 1992).

Using the method of operator splitting, we first find out the differenced form of the equation,

$$\frac{\partial g(x, t)}{\partial t} \equiv V(x) \frac{\partial g(x, t)}{\partial x}, \quad (5.22)$$

by upwind *differencing*, to obtain,

$$g_j^{n+1} = g_j^n + \frac{\delta t}{\delta x} V_j (g_j^n - g_{j-1}^n), \quad (5.23)$$

where, δt and δx represent the time interval and the size of the space-grid. The superscript n stand for the n -th time-step and the subscript j stand for the j -th space-grid of integration. Similarly, for the diffusive part, given by,

$$\frac{\partial g(x, t)}{\partial t} = S(x, t) \left(\frac{\partial^2 g(x, t)}{\partial x^2} - \frac{2g(x, t)}{x^2} \right) \quad (5.24)$$

we use Crank-Nicholson scheme to obtain,

$$g_j^{n+1} = g_j^n + \frac{\delta t S_j^{n+1/2}}{2(\delta x)^2} (g_{j+1}^{n+1} - 2g_j^{n+1} + g_{j-1}^{n+1} + g_{j+1}^n - 2g_j^n + g_{j-1}^n) - \frac{2\delta t S_j^{n+1/2} g_j^n}{x_j^2}, \quad (5.25)$$

where the various symbols have the same meaning as in equation [5.23]. To incorporate the time-dependence of $S(x, t)$ without making the differencing scheme too complicated, we use the time-averaged (over two neighbouring intervals) value of the function at each time-step. This does not introduce too much error as the function is slowly-varying over the time-intervals typically chosen for our integrations. In the end we combine the schemes in the following manner,

$$\begin{aligned} g_j^{n+1} &= g_j^n + \frac{\delta t}{\delta x} V_j (g_j^n - g_{j-1}^n) \\ &+ \frac{\delta t S_j^{n+1/2}}{2(\delta x)^2} (g_{j+1}^{n+1} - 2g_j^{n+1} + g_{j-1}^{n+1} + g_{j+1}^n - 2g_j^n + g_{j-1}^n) \\ &- \frac{2\delta t S_j^{n+1/2} g_j^n}{x_j^2}, \end{aligned} \quad (5.26)$$

to obtain the final differenced form of the equation [5.16] which is used in the numerical code.

In connection with the numerical code an important point needs to be mentioned. It is imperative, before it is used to obtain results, to check for the stability of the numerical scheme employed. The Crank-Nicholson scheme of differencing is unconditionally stable for any size of the temporal or spatial grid. Hence any instability in our scheme arises from the convective part for which the scheme used (upwind differencing) is, unlike the

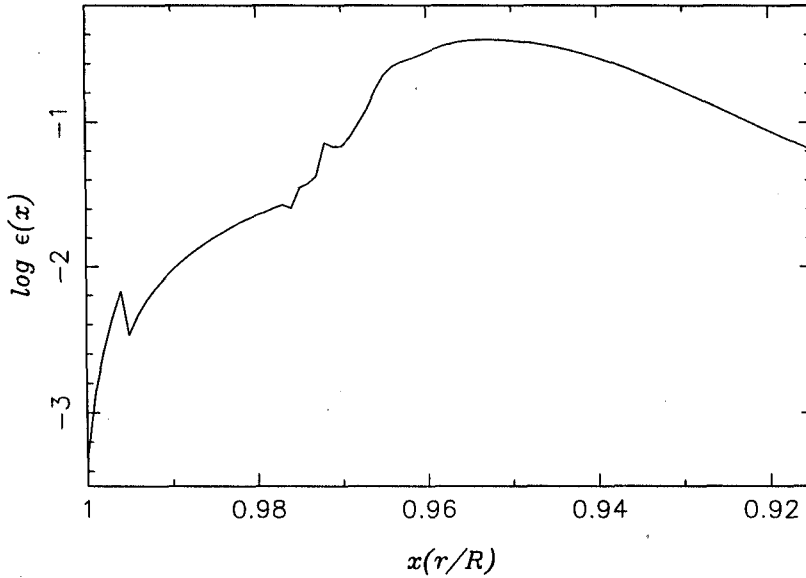


Figure 5.1: ϵ as a function of the fractional radius x .

other scheme, not stable for all combinations of the spatial and temporal intervals. The stability of this scheme depends on whether the Courant condition is satisfied or not. This condition demands that the inequality

$$\frac{\delta t}{\delta x} V(x) \lesssim 1, \quad (5.27)$$

be satisfied at all grid points and at all points of time. Using equations [5.11] and [5.21] to arrive at the values of $V(x)$ for a given rate of accretion and for a space-grid of 100 points we find that for an accretion rate of $10^{-8} M_{\odot} \text{ yr}^{-1}$ (which is roughly the Eddington rate of accretion for a $1.4 M_{\odot}$ neutron star) the maximum time-interval allowable by the Courant condition is 10^{-2} years. This of course places a severe constraint on computational resources in terms of run-time.

In equation [5.16] above, the convective and the diffusive terms dominate the evolution in different density ranges. To illustrate this fact, similar to the diffusive time-scale defined in equation [5.10], we define a convective time-scale :

$$\tau_{\text{conv}} = \frac{L}{V(r)} \quad (5.28)$$

where L is the system size as before. In figure [5.1] we plot the relative magnitude of these two time-scales defined by the coefficient,

$$\epsilon = \frac{\tau_{\text{diff}}}{\tau_{\text{conv}}}. \quad (5.29)$$

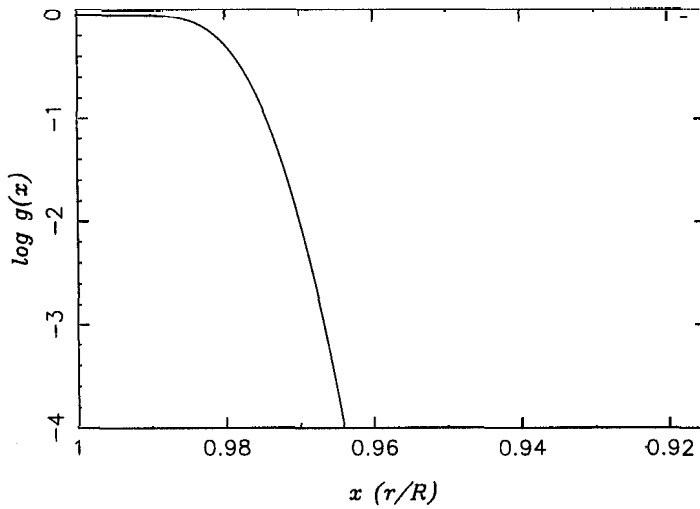


Figure 5.2: The initial radial dependence of the g -profile centered at $x = 0.98$, which corresponds to $\rho = 10^{11} \text{ g cm}^{-3}$, with a width $\delta x = 0.006$; where x is the fractional radius r/R .

This plot is made for an assumed accretion rate of $10^{-9} M_{\odot} \text{ yr}^{-1}$. It is clear from this figure that both in the low density regions near the surface and in the deep high density regions it is the diffusive term that is more important. Only in the intermediate regions the effect of convection becomes significant.

5.4 results and discussions

The results are summarized in a series of figures.

Figure [5.2] shows the distribution of the g -function and figure [5.3] the toroidal currents, J_{ϕ} , assumed at the starting point of the field evolution.

Field decay due to pure diffusion in an isolated neutron star is shown in figures [5.4] and [5.6]. In computing this, neutron star cooling according to the results of van Riper (1991a,b) (reproduced here in figure [5.5]) for normal matter in $1.4 M_{\odot}$ Friedman & Pandharipande (1981) model star has been used. It is to be noted that our adopted equation of state, namely, that of Wiringa, Fiks & Fabrocini (1988) is an updated version of Friedman & Pandharipande equation of state with only minor differences.

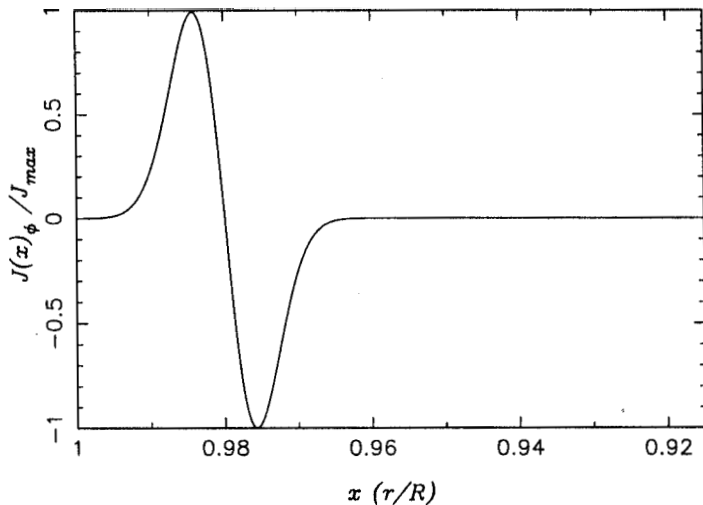


Figure 5.3: The initial radial dependence of the ϕ -component of the corresponding current configuration.

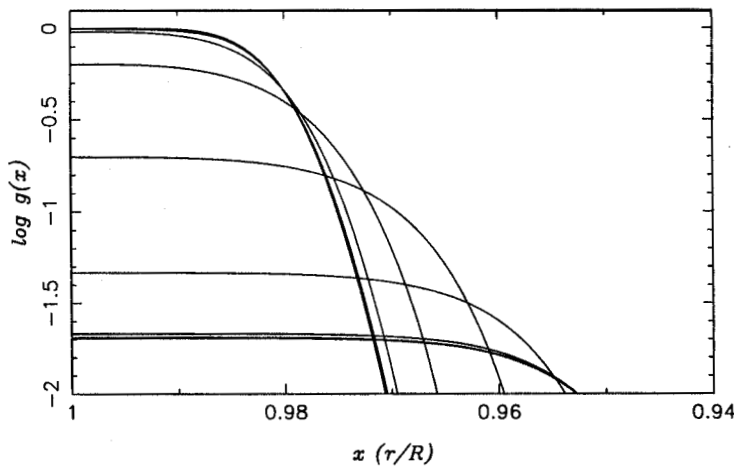


Figure 5.4: Pure ohmic diffusion of the g -profile for $\tau \sim 10^9$ yrs, centred at $\rho = 10^{11} \text{ g cm}^{-3}$, with $Q = 0.0$, in a neutron star with standard cooling. The curves shown at intermediate times correspond to, $t = 10, 10^2, 10^3, 10^4, 10^5, 10^6, 10^7, 10^8, 10^9$ years (the last three are almost indistinguishable), respectively, with decreasing values at the surface ($x = 1$).

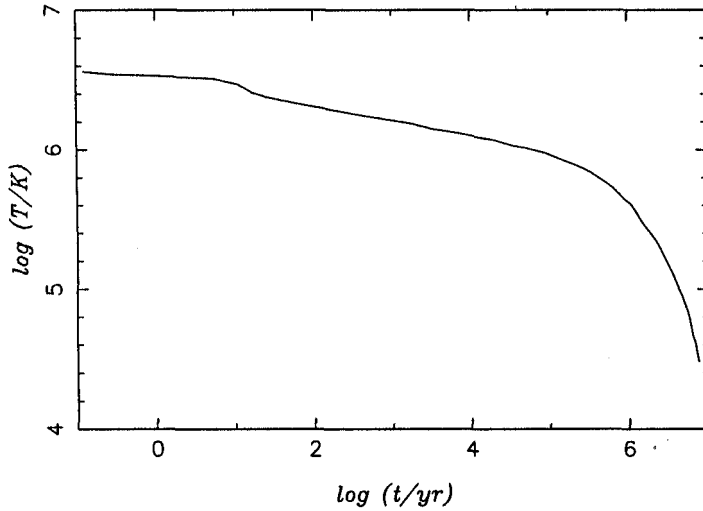


Figure 5.5: Evolution of the Neutron Star core temperature, after van Riper (1991a,b).

Among the published cooling curves this is the nearest to that appropriate to our adopted neutron star model. Computations similar to the one displayed in figures [5.4] and [5.6] have been made by Urpin & Muslimov (1992) and our result matches very closely with theirs. It is evident from the figure [5.6] that the net decay decreases with the increasing density at which the initial current configuration is centred at. This is expected as the diffusive time-scales are larger at higher densities owing to larger conductivities there.

Figure [5.7] displays the result of the convection due to material movement alone. We obtain this by setting the conductivity α to an artificially high value of 10^{50} s^{-1} in our code. It shows the migration of g -profile to regions of higher density (and consequent sharpening of the profile). The field at the surface ($B_s = 2g(R, t)/R^2$) remains constant under pure convection according to our assumptions.

Figure [5.8] shows the results of the combined effects of convection and diffusion on the g -function, in other words the full evolution described by equation [5.16], for a particular value of the accretion rate.

In section [5.2.2] we have mentioned that accretion induces compression of the crustal layers and hence effect a reduction of the effective length-scale of the current profile.

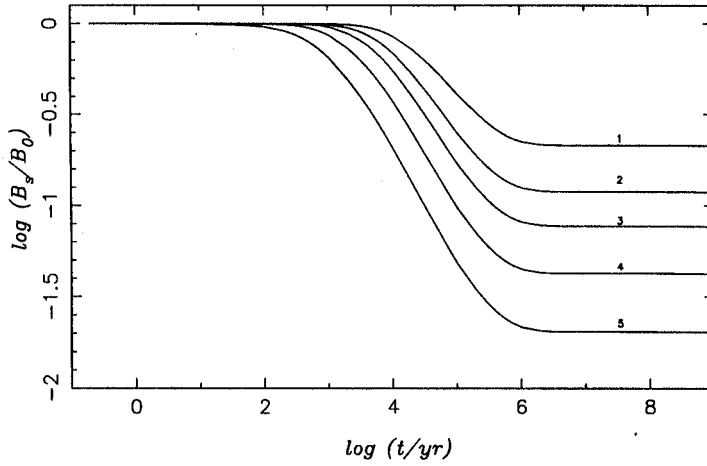


Figure 5.6: The evolution of the surface magnetic field due to pure diffusion. Curve 5 in this figure correspond to the g-profile plotted in figure [5.4]. Curves 1 to 4 correspond to $10^{13} \text{ g cm}^{-3}$, $10^{12.5} \text{ g cm}^{-3}$, $10^{12} \text{ g cm}^{-3}$ and $10^{11.5} \text{ g cm}^{-3}$ respectively, at which the g-profiles are centred. All curves correspond to $Q = 0$.

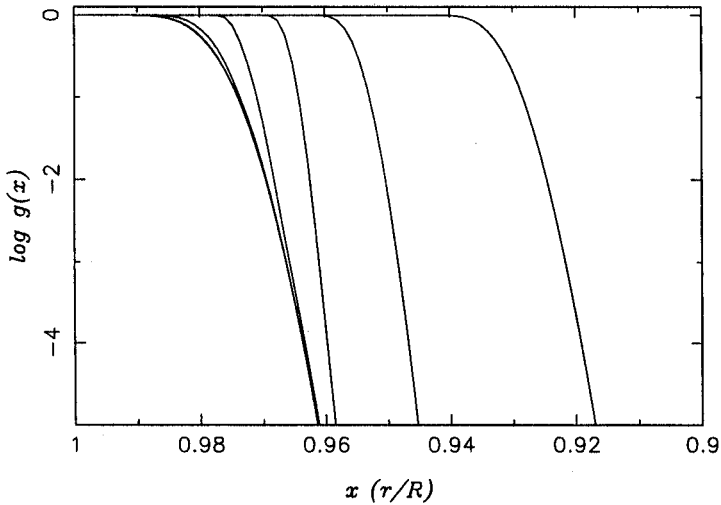


Figure 5.7: Convective transport of the g-profile over 10^9 years with $M = 10^{-10} M_{\odot} \text{ yr}^{-1}$, surface field is constant by assumption. The curves shown at intermediate times correspond to, $t = 10, 10^2, 10^3, 10^4, 10^5, 10^6, 10^7, 10^8, 10^9$ years (the first four are barely distinguishable), respectively, with the profiles progressively moving inwards.

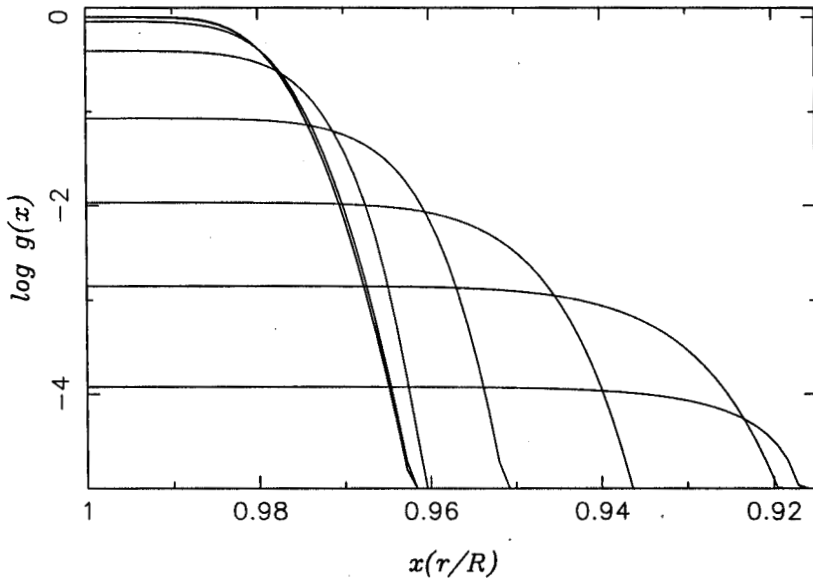


Figure 5.8: Evolution of the g -profile due to ohmic diffusion and convective transport, over a period of 10^6 years for $\dot{M} = 10^{-9} M_{\odot}/\text{yr}$, $T = 10^{8.0}$ K and $Q = 0.0$. The curves shown at intermediate times correspond to, $t = 10^2, 10^3, 10^4, 10^5, 10^6, 10^7, 4.0 \times 10^7$ years, respectively, with decreasing values at the surface ($x = 1$).

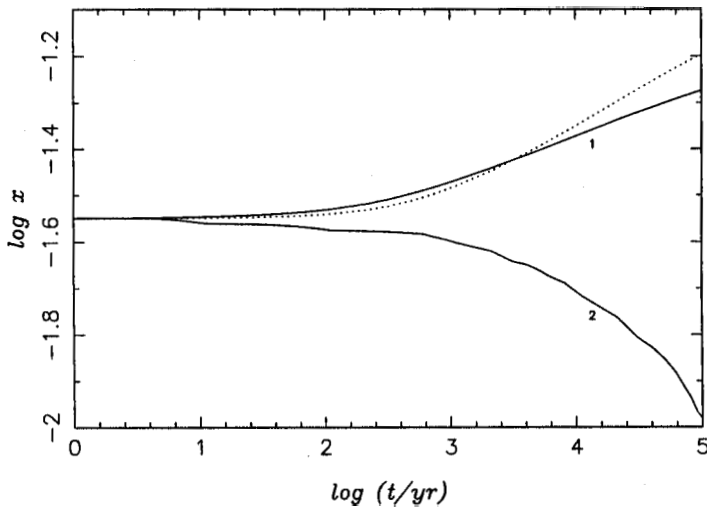


Figure 5.9: Evolution of the length scale (in fractional radius) of the g -profile over a period of 10^5 years. Curve 1 correspond to pure ohmic diffusion with standard cooling and $q = 0$. Curve 2 correspond to pure convection with an accretion rate of $\dot{M} = 10^{-10} M_{\odot}/\text{yr}$ and the dotted curve corresponds to the case of actual accretion with the same \dot{M} .

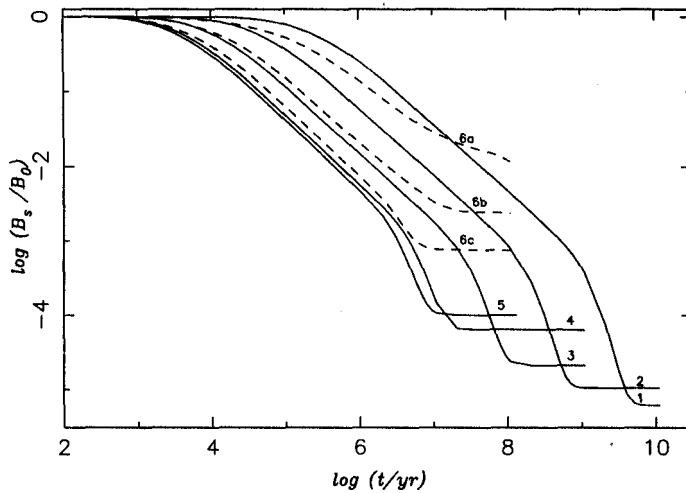


Figure 5.10: Evolution of the surface magnetic field for six values of accretion rate. The curves 1 to 5 correspond to $M = 10^{-13}, 10^{-12}, 10^{-11}, 10^{-10}, 2.0 \times 10^{-10} M_{\odot} \text{ yr}^{-1}$ with the crustal temperatures obtained from equation [2.13]. The dashed curves 6a, 6b and 6c correspond to $T = 10^{8.0}, 10^{8.25}, 10^{8.5}$ K respectively for an accretion rate of $M = 10^{-9} M_{\odot} \text{ yr}^{-1}$. All curves correspond to $Q = 0.0$, but are insensitive to the value of Q .

In figures [5.4], [5.7] and [5.8] we have seen how the g-profile evolves due to pure diffusion, pure convection and a combination of both. Here, in figure [5.9] we plot the change of the length-scale of the g-profile with time in each of the above-mentioned cases. As an estimate of the effective length-scale of the current distribution we use the width (defined as the separation between the peak of the distribution and a point which has 1% of the peak magnitude) of the g-profile. Though this is but a crude estimate, it nevertheless serves the purpose of illustrating the qualitative nature of the change of the length-scale. The curves for pure diffusion and pure convection show monotonous increase and decrease respectively. Even though the curve for the case of actual accretion (where both diffusion and convection are present) the nature is again that of a monotonic increase in length scale similar to the case of pure diffusion, it rises comparatively slowly initially. This is due to the fact that the convective compression slows the diffusive spreading. Of course, in the end the diffusive spreading becomes faster than the case of pure diffusion due to heating which lowers the conductivity.

In figure [5.10] we display the evolution of the surface field for different values of M ,

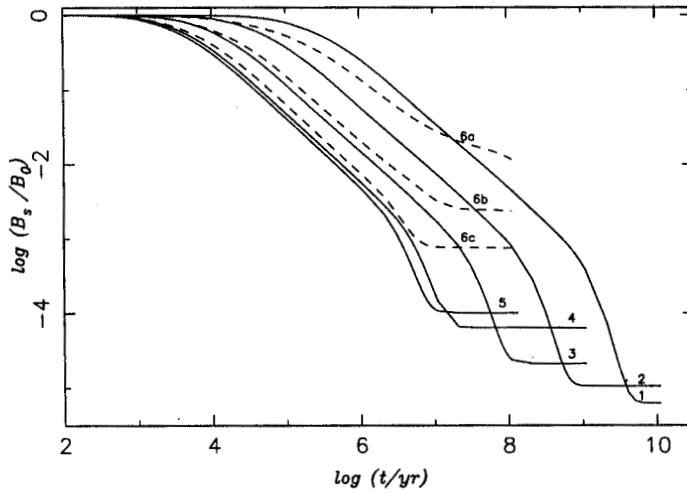


Figure 5.11: Same as figure [5.10] with the initial profile centred at $10^{11.5} \text{ g cm}^{-3}$.

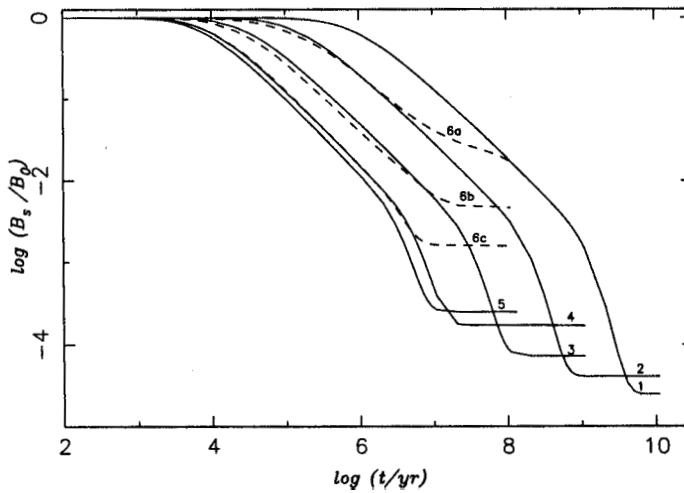


Figure 5.12: Same as figure [5.10], with the initial g-profile centred at $10^{12} \text{ g cm}^{-3}$.

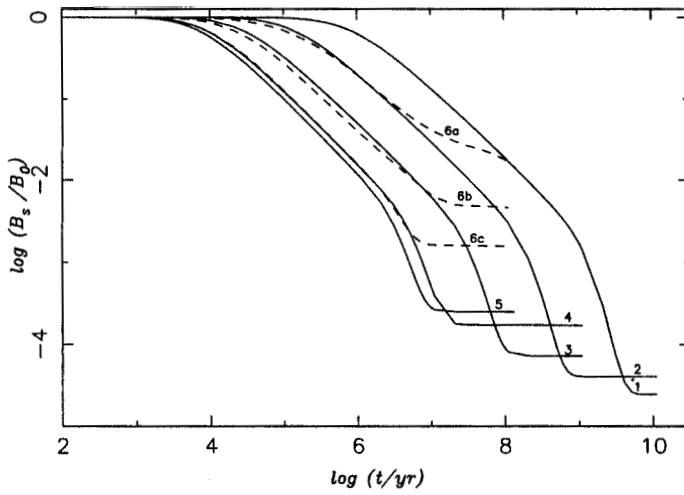


Figure 5.13: Same as figure [5.10], with the initial g-profile centred at $10^{12.5} \text{ g cm}^{-3}$.

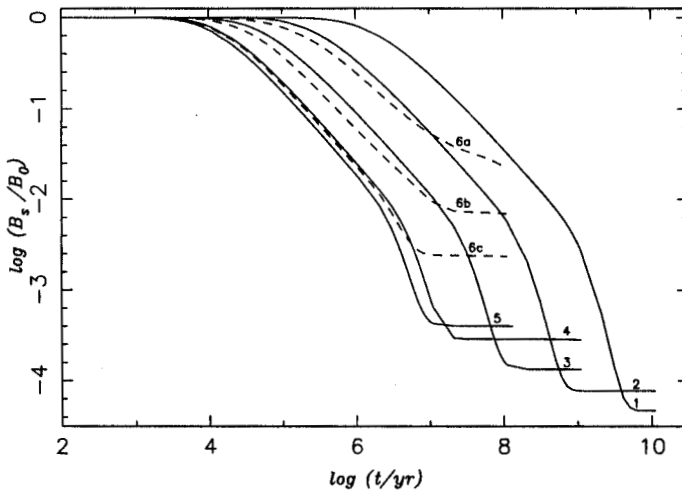


Figure 5.14: Same as figure [5.10], with the initial g-profile centred at $10^{13} \text{ g cm}^{-3}$.

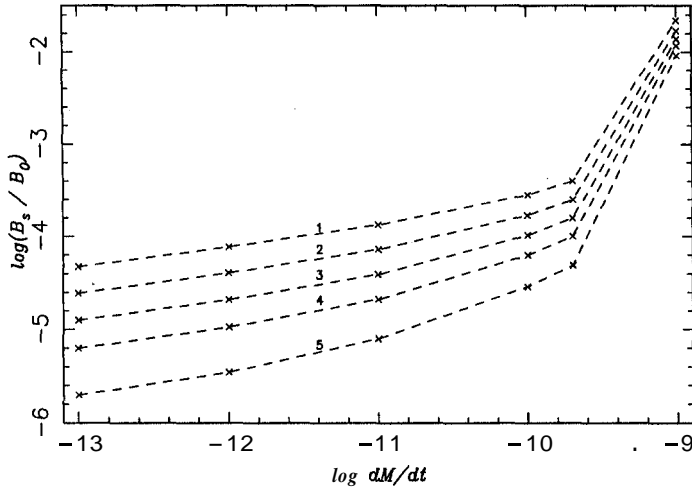


Figure 5.15: Final surface field vs. rate of accretion. Curves 1 to 5 correspond to the initial g-profile centering densities of 10^{11} , $10^{11.5}$, 10^{12} , $10^{12.5}$, 10^{13} g cm^{-3} respectively. For the accretion rate of $M = 10^{-9} M_{\odot} \text{ yr}^{-1}$, we have used the values corresponding to the crustal temperature of 10^8 K.

with temperatures obtained from equation [2.13] over its validity range and for three different assumed temperatures at the highest accretion rate. All the curves in this figure refer to an initial g-profile that is centred at a density of $10^{11} \text{ g cm}^{-3}$. In figures [5.11], [5.12], [5.13] and [5.14] we plot similar curves for different densities at which the initial current profiles are centred. In figure [5.15] we display the final surface field values obtained as a function of the rate of accretion for different values of initial current concentration densities.

The following features emerge from the behaviour displayed in these figures:

1. The general nature of the decay corresponds to an initial rapid phase exhibiting a power law behaviour for the most part with an index ranging from 0.1 to 0.46 (i.e., $B \sim t^{-n}$, $0.1 \lesssim n \lesssim 0.46$), followed by a short exponential phase and then a freezing, which stabilizes the surface field. This stability is the result of the current distribution responsible for the field moving to highly conducting parts of the star, much of it migrating into the core. According to our adopted scenario, the ohmic time scale in the core is much longer than the Hubble time and hence the surface field at this stage will essentially be stable forever. We refer to this surface field as the '*residual* field'.

2. The duration of the exponential phase and consequently the value of the magnetic field at which freezing occurs is a strong function of the accretion rate. The higher the accretion rate the sooner the freezing sets in resulting in a higher value of the 'residual field'. This effect can be understood as follows. As explained by Bhattacharya (1995a) the decay behaviour turns from a power law to an exponential, once the diffused g-distribution reaches nearly the bottom of the crust. The transition from there to the frozen state happens by further accretion of matter which pushes the crustal material into the core. The time required for this final transition is of course dependent on the accretion rate and the higher the accretion rate the smaller it is. For a rate of accretion of $10^{-9} M_{\odot}/\text{yr}$, this exponential phase is nearly absent.
3. The dependence of the decay on the crustal temperature is as expected, namely, the decay proceeds faster at a higher temperature.
4. In figure [5.15] we have plotted the final 'frozen field' for different rates of accretion corresponding to different densities at which the initial current profile is centred at. It is clearly seen from this figure that the lower the rate of accretion, the lower is the final 'frozen in' field.
5. In figure [5.16] the evolution of the surface magnetic field as a function of total accreted mass has been plotted for different rates of accretion. Corresponding to a given accretion rate the crustal temperature has been obtained from equation [2.13]. It is observed that the *freezing in* of the field occurs for larger accreted mass for higher rates of accretion. The high accretion rate also ensures quicker material transport to higher densities, causing the field strength to level off at a higher value. Another important point to note here is that unlike what is assumed in heuristic evolutionary models (Taam & van den Heuvel 1986; Shibasaki et al. 1989; van den Heuvel & Bitzaraki 1995) the amount of field decay is dependent not only on the total mass accreted but also on the accretion rate itself. Once the accreted mass exceeds $\sim 10^{-3} M_{\odot}$, the final magnetic field strength is decided only by the rate at which this mass was accreted. Whereas figure [5.16] correspond to an initial profile centred at $10^{11} \text{ g cm}^{-3}$, in the figures [5.17], [5.18], [5.19] and [5.20] we plot similar curves for different densities.
6. In practice a neutron star will often undergo a non-accreting phase of considerable duration before accretion can begin on its surface. During this initial phase its magnetic field will evolve as in an isolated neutron star, namely according to the

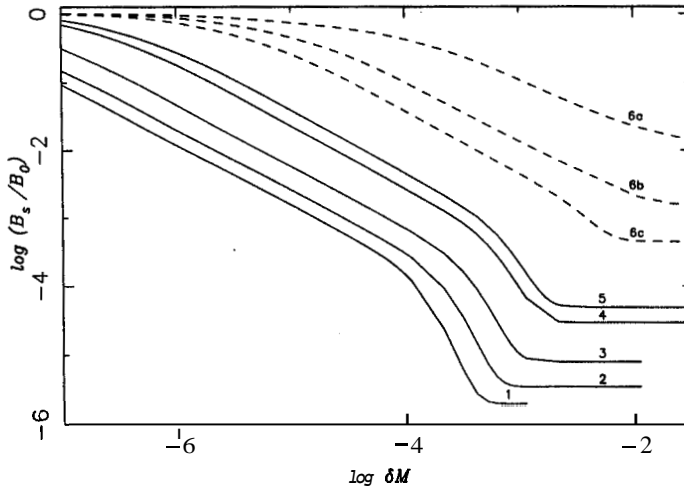


Figure 5.16: Evolution of the surface magnetic field as a function of total mass accreted. The curves 1 to 6 correspond to $M = 10^{-9}, 2.0 \times 10^{-10}, 10^{-10}, 10^{-11}, 10^{-12}, 10^{-13} M_{\odot} \text{ yr}^{-1}$, the crustal temperatures are obtained from equation [2.13]. The dashed curves 6a, 6b and 6c correspond to $T = 10^{8.0}, 10^{8.25}, 10^{8.5} \text{ K}$ respectively for an accretion rate of $M = 10^{-9} M_{\odot} \text{ yr}^{-1}$. All curves correspond to $Q = 0.0$. and an initial profile centred at $10^{11} \text{ g cm}^{-3}$.

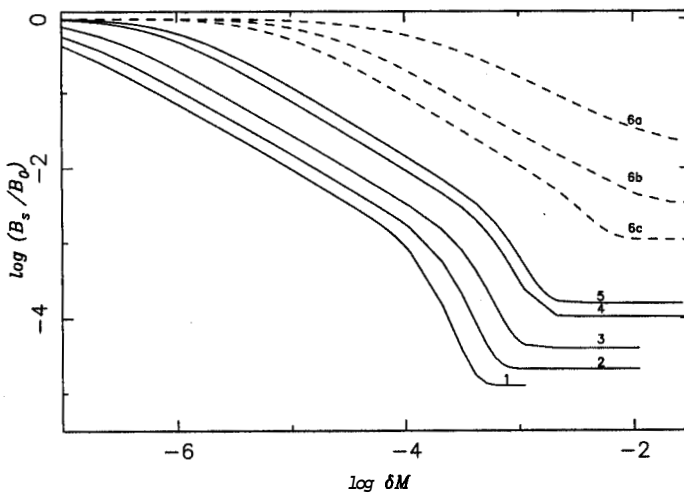


Figure 5.17: Same as figure [5.16], with the initial g-profile centred at $10^{12} \text{ g cm}^{-3}$.

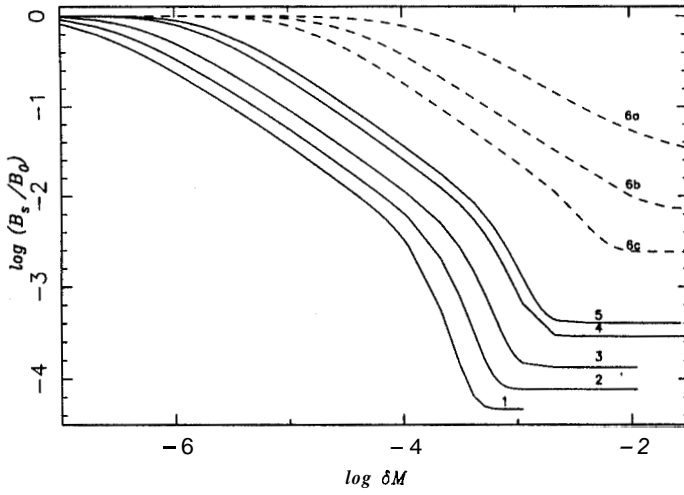


Figure 5.18: Same as figure [5.16], with the initial g-profile centred at 10^{12} g cm $^{-3}$.

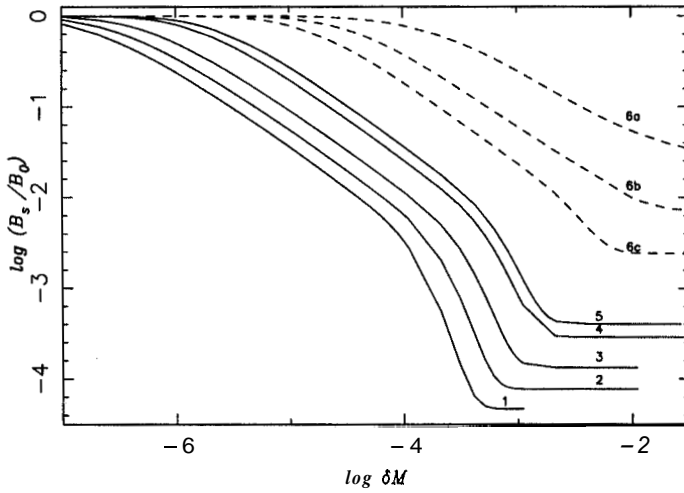


Figure 5.19: Same as figure [5.16], with the initial g-profile centred at $10^{12.5}$ g cm $^{-3}$.

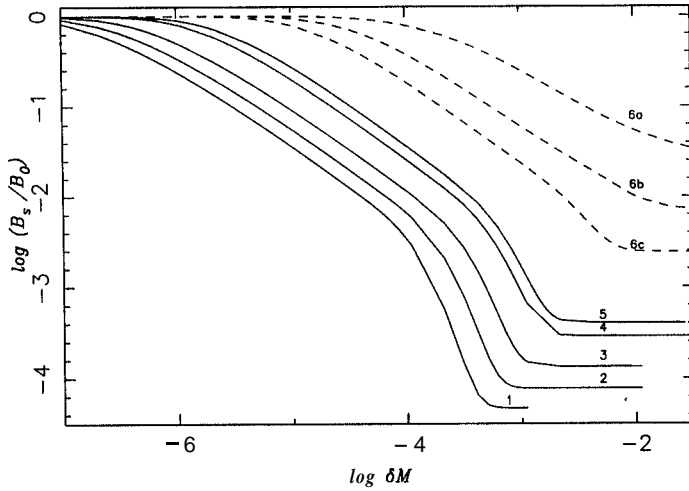


Figure 5.20: Same as figure [5.16], with the initial g-profile centred at $10^{13} \text{ g cm}^{-3}$.

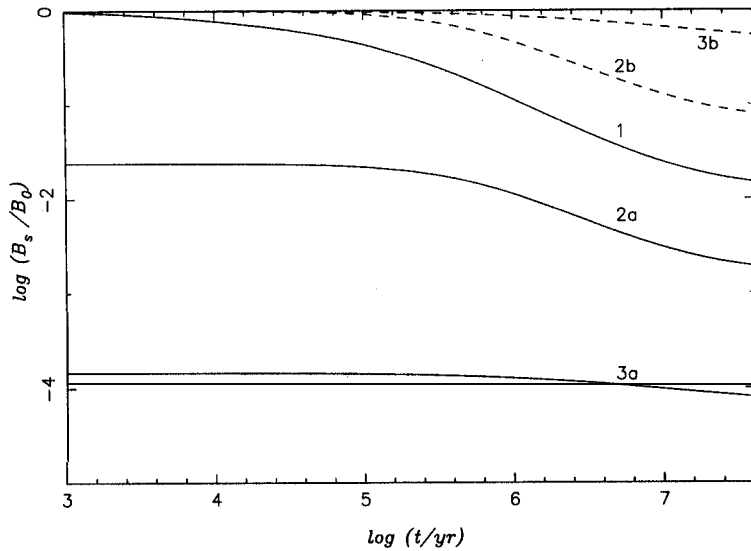


Figure 5.21: Evolution of the surface magnetic field (1) without any pre-accretion phase and (2 & 3) for such a phase lasting $\sim 10^9$ yrs. In all cases $\dot{M} = 10^{-9} M_{\odot} \text{ yr}^{-1}$, and $T = 10^{8.0} \text{ K}$. $Q = 0.0$ for curves 1, 2a, 2b and $Q = 0.1$ for 3a, 3b. In 2a and 3a the actual surface field has been plotted, whereas in 2b and 3b it has been scaled to the value of the field at the beginning of the accretion phase. In the isolated phase standard cooling van Riper (1991a,b) has been used.

evolution shown in figure [5.6]. This has important physical consequences for the evolution in the accretion phase. The diffusion in the pre-accretion phase causes the currents to already penetrate to deeper and denser regions of high conductivity. As a result the net decay achieved during subsequent accretion is lower. Figure [5.21] compares the evolution of the surface field without and with the pre-accretion phase lasting a billion years. It should also be noted that for accretion-induced field decay with an effectively isolated pre-accretion phase, the impurity concentration plays an important role too. Though the actual final field values obtained is lower for large Q , the decay experienced in the accretion phase is significantly less in such cases and the 'freezing' sets in much faster.

7. As mentioned before, the range of conditions explored by us overlap with those in the work of Urpin & Geppert (1995, 1996), Urpin, Geppert & Kononov (1996) and goes beyond. We have performed detailed comparisons of our results with theirs in the overlap range. The agreement in general is found to be excellent giving us confidence in the validity of our approach.

To summarize, we have explored accretion-driven evolution of crustal magnetic fields over a range of conditions not previously attempted in the literature. The new behaviour revealed by these computations include a near exponential decay of the surface field after the initial power law phase and most importantly an eventual freezing. The 'residual field' corresponding to this frozen state is a function of the accretion rate and the temperature during the evolution. It is interesting to note that for near-Eddington accretion rates, applicable to Roche-lobe overflow phase in real binaries, the 'residual field' lies between 10^{-2} – 10^{-4} of the original value. So, if the neutron star originally started with a field strength of the order of 10^{12} G, this would mean a final post-accretion field strength of 10^8 – 10^{10} G, exactly as observed in most recycled pulsars. Unfortunately, we have not been able to treat accretion rates equal to or larger than Eddington in the present work due to lack of knowledge about the crustal temperatures at those accretion rates. But judging by the dependence of the behaviour on accretion rates (see figure 5.151) it appears that even somewhat higher post-accretion field strengths might be possible under such conditions. Recycled pulsars with the strongest magnetic fields, namely PSR 0820+02 and PSR 2303+46 have, according to evolutionary scenarios (see, e.g., Bhattacharya & van den Heuvel 1991), undergone super-Eddington mass transfers. Their field strengths would therefore be in agreement with the trend described above.

5.5 conclusions

In this chapter we have explored the evolution of the crustal magnetic field of accreting neutron stars. The combination of enhanced ohmic diffusion due to crustal heating and the transport of current-carrying layers to higher densities due to the accreted overburden, causes the surface field strength to exhibit the following behaviour:

1. An initial rapid decay (power law behaviour followed by exponential behaviour) followed by a leveling off (freezing),
2. Faster onset of freezing at higher crustal temperatures and at a lower final value of the surface field,
3. Lower final fields for lower rates of accretion for the same net amount of accretion,
4. The longer the duration of the pre-accretion phase the less the amount of field decay during the accretion phase, and
5. The deeper the initial current loops are the higher the final surface field.

Chapter 6

comparison with observations

6.1 introduction

In the previous chapter we have discussed a model for the evolution of the magnetic field in accreting neutron stars, assuming an initial crustal **flux**. It has been borne out by our calculations that the model possesses some essential features required to explain the origin of the observed low-field pulsars. But in a broader perspective it is also necessary for a model to explain the present paradigm of the field evolution in its entirety. The astronomical objects that have so far been unambiguously identified with neutron stars can be divided into two distinct classes :

- the radio pulsars, and
- the X-ray binaries containing a neutron star.

Interestingly, observations suggest that a class of radio pulsars descend from X-ray binaries, and neutron stars in X-ray binaries themselves represent an evolutionary state beyond that of isolated radio pulsars (see Bhattacharya 1995b, 1996a, van den Heuvel 1995, Verbunt & van den Heuvel 1995 and references therein). Therefore the present belief is that this evolutionary link can be understood within an unified picture of evolution of their spin as well as the magnetic field. The spin-evolution of the neutron stars in binary systems have been investigated following the detailed binary evolution assuming some simple model for the field evolution (see Verbunt & van den Heuvel 1995 and references therein). In the present work we concentrate on the details of the evolution of the magnetic field. We apply the model of field evolution to isolated neutron stars as well as to those that are members of binaries. Comparison of these results with observations allows us to test the validity of the field evolution model.

Radio pulsars can be classified into two groups, namely the solitary pulsars and the binary pulsars. The binary pulsars are again of two types - the high mass binary pul-

sars and the low mass binary pulsars, the reference to the masses being to those of the companions. It has been suggested by recent statistical analyses that the fields of the isolated neutron stars do not undergo any significant decay (Ruderman 1991(a,b,c), Bhattacharya & Srinivasan 1991, Ding et al. 1993, Jahan Miri & Bhattacharya 1994, Jahan Miri 1996). On the other hand almost all binary pulsars possess field values that are smaller than the canonical field values observed in isolated pulsars. Usually the high mass binary pulsars, of which the Hulse-Taylor pulsar is one famous example, have field strengths in excess of 10^{10} Gauss, whereas the low mass binary pulsars include both high-field pulsars and very low-field objects like the millisecond pulsars. It must be noted here that when we talk about the solitary pulsars we mean high-field solitary pulsars without any history of binary association. The millisecond pulsars and pulsars with obvious or suspected binary history are discussed along with their binary counterparts for the sake of convenience. The present belief regarding the evolutionary history of the binary pulsars is that the high mass binary pulsars come from systems similar to the high mass X-ray binaries whereas the low mass binaries are the progenies of the low mass X-ray binaries. In the following table we present this evolutionary scenario.

systems	solitary pulsars (millisecond pulsars) excluded)	high mass binary pulsars	low mass binary pulsars
companion		neutron stars, massive ($\gtrsim 0.6 M_{\odot}$) white dwarfs	low mass stars low mass ($\lesssim 0.4 M_{\odot}$) white dwarfs
magnetic field	$10^{11} - 10^{13}$ Gauss	usually $\gtrsim 10^{10}$ Gauss	$10^8 - 10^{11.5}$ Gauss
progenitors		high mass X-ray binaries	low mass X-ray binaries

Even though the millisecond pulsars fall in the broader category of low mass binary pulsars, we shall mention them separately due to their unique characteristic features. The rotation powered radio pulsars separated out into two distinct classes with the discovery of the 1.6 ms pulsar, PSR 1937+21 (Backer et al. 1982). In accordance with

the extremely small rotation periods (\sim ms) of this new variety they came to be known as *Millisecond Pulsars* as opposed to the population of normal pulsars that have longer rotation periods. Loosely, the term millisecond pulsar refers to the class of pulsars with rotation periods less than 20 ms. This definition, though somewhat ad-hoc, actually serves the purpose of classification rather well. In other words, all the members of the class of millisecond pulsars show remarkable similarity in several of their characteristic physical properties (listed below), which also serve to distinguish them from the rest of the pulsar population.

The characteristic features of the millisecond pulsars could be summarized as follows.

1. fast rotation – $P \lesssim 20$ ms;
2. extremely small magnetic fields (three to four orders of magnitude smaller than the canonical field values observed in normal pulsars) – $B \sim 10^8 - 10^9$ G;
3. binary association – 90% of the disc population and 50% of the Globular Cluster population of the millisecond pulsars have low-mass binary companions, with most probable mass of the companion $\lesssim 0.3M_{\odot}$, in nearly circular orbits;
4. old age – age determination from the presence in the Globular Cluster or from the surface temperature measurements of a white dwarf companion (e.g., for PSR 1855+09) indicate a lifetime of 10^9 years or more (Hansen & Phinney 1997).

It has been shown that a total mass of $\sim 0.1M_{\odot}$ is required to be accreted to achieve millisecond period through accretion induced spin-up. Present theories of binary evolution predict that the only systems capable of supporting mass-transfer long enough (about 10^7 years at the Eddington rate of accretion) to allow the neutron stars to accrete $\gtrsim 0.1 M_{\odot}$ are the ones with low-mass ($\lesssim 1.5 M_{\odot}$) donors (the Low Mass X-ray Binaries or LMXBs in short). Hence, it is generally believed that the evolutionary link between a normal radio pulsar and its millisecond counterpart is through a phase of binary processing in LMXBs. In general the companion of a binary pulsar is indicative of the system from which it originated. A pulsar with neutron star or a massive ($\gtrsim 0.6 M_{\odot}$) white dwarf companion is understood to have come from a system containing a massive ($\gtrsim 5 M_{\odot}$) donor. Similarly, a pulsar with a low mass ($\lesssim 0.4 M_{\odot}$) white dwarf companion must originate in a low mass X-ray binary. All the binary millisecond pulsars have low mass companions, indicating their origin in low-mass systems.

At this stage, it becomes imperative that the models for evolution of the magnetic field be consistent with the spin-evolution scenario. There is, as yet, no consensus about the

models of field evolution or about those of the origin and structure of the field. Based on the two theories of field generation and the corresponding internal structures (see section [3.2]) one can broadly classify the models of field evolution into two categories. The original theory of recycling assumed a spontaneous ohmic decay of magnetic field with age, which according to the present evidence, appears unlikely. For a magnetic flux confined to the core, the model of spindown-induced flux expulsion has been explored (Jahan Miri & Bhattacharya 1994; Jahan Miri 1996; Bhattacharya & Datta 1996). We shall discuss this model in the next chapter.

In this chapter, we confront the field evolution model of chapter [5], namely that of assuming an initial crustal flux, with observations of both isolated neutron stars and neutron stars in binary systems. In particular, we address the question of millisecond pulsar generation purely from the point of view of the field evolution. Our results are consistent with the general view that millisecond pulsars come from low mass x-ray binaries. We also find that the neutron stars processed in high mass x-ray binaries would retain fairly high field strengths in conformity with what is observed in high mass radio pulsars.

In section [6.3] we discuss the nature of field evolution of a neutron star vis-a-vis the binary evolution of the system which it is a member of. Section [6.4] elaborates the computational details. We present our results in section [6.5] and the conclusions in section [6.6].

6.2 field evolution in solitary neutron stars

According to modern statistical analyses (Bhattacharya et al. 1992, Wakatsuki et al. 1992, Hartman et al. 1997) the isolated neutron stars do not undergo any significant field reduction over their active pulsar life time. In an isolated neutron star the field decreases due to pure ohmic dissipation of the current loops in the crust. We have already mentioned that the diffusive time-scale is dependent on three factors, namely

- the density at which the initial current loops are located,
- the impurity content of the crust, and
- the temperature of the crust.

We shall look at the effect of all these factors and determine the acceptable ranges for these parameters for which the final field strengths are within the limits of statistical

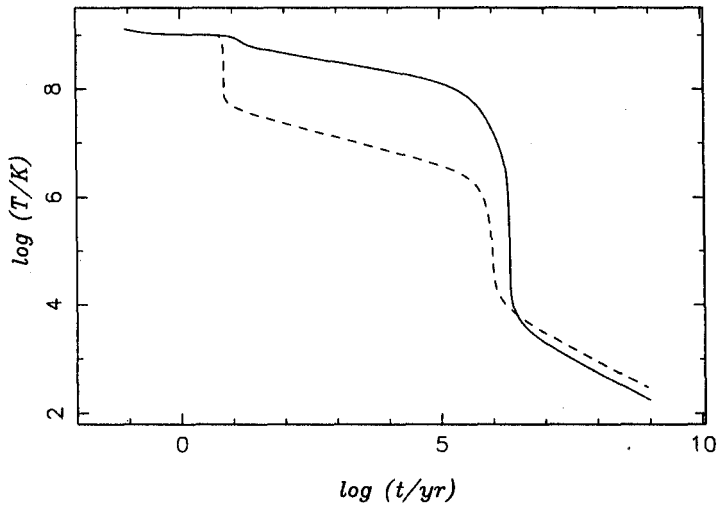


Figure 6.1: Evolution of the interior temperature of an isolated neutron star. The solid and dotted curves correspond to standard cooling and accelerated cooling, respectively.

uncertainty.

An isolated neutron star cools down after its birth chiefly by copious neutrino emission. It has recently been shown (see Page, 1997 and references therein for details) that there are lots of uncertainties in this regard. The data could be made to fit both the 'standard' cooling and the 'accelerated' cooling with appropriate assumptions regarding the state of the stellar interior. Therefore, for the sake of completeness, we have looked at both the cases - with standard and accelerated cooling. The actual behaviour of the system is most likely to be something in between. We have used data from Urpin & van Riper (private communication) for both standard and accelerated cooling. In figure [6.1] the two cooling curves have been shown for a comparison.

6.3 field evolution in neutron stars with binary companions

6.3.1 binary and spin evolution

From the point of view of the interaction between the two stars, the binaries, in general, go through three distinct phases of evolution as detailed below.

1. The Isolated Phase - Though the stars are gravitationally bound, there is no mass transfer. Therefore both the spin and the magnetic field evolve as they would in an isolated pulsar. The spin undergoes a pure dipole slow-down during this phase.
2. The Wind Phase - The interaction is through the stellar wind of the companion which is likely to be in its main-sequence. In this phase the interaction of the wind material with the magnetosphere of the neutron star proceeds in two distinct sequences. In the early stages of the wind phase the magnetospheric interaction brings about a spin-down of the neutron star in the following manner. In the accretion disc the matter rotates with a Keplerian velocity at every point within the disc. When the matter arrives at the magnetospheric boundary of the star (determined roughly by the Alfvén radius where the magnetic pressure equals the ram pressure of the incoming material) the magnetic field starts controlling the material flow dynamics. This point onwards the field forces the material to co-rotate with the star. If the Keplerian velocity of the incoming material is smaller than the co-rotation velocity at the Alfvén radius then the material, in being forced to co-rotate with the star there, extracts angular momentum from the star thereby slowing it down. This material then gets expelled from the magnetosphere which has given this situation the name *propeller phase*. For 'spin-down induced flux expulsion' models the 'propeller phase' is the most crucial for the field evolution because it is in this phase that a significant flux expulsion is achieved due to a rapid spin-down of the star. Once the star has been spun-down sufficiently the Keplerian velocity at Alfvén radius becomes larger than the co-rotation velocity. In this case the accreting material loses angular momentum as it reaches Alfvén radius, spinning the star up. This material eventually reaches the polar cap of the star by moving along the field lines and gets deposited there. Therefore, this is the phase in which there is actual mass accretion by the star. An equilibrium is reached when the co-rotation speed equals the Keplerian speed at the magnetospheric boundary, i.e, at the Alfvén radius. This equilibrium condition then determines the maximum spin-up for a given rate of accretion and a given strength of the surface field, through the following relation (Alpar, Cheng, Ruderman & Shaham 1982, Chen & Ruderman 1993)

$$P_{\text{eq}} = 1.9 \text{ ms } B_9^{6/7} \left(\frac{M}{1.4M_\odot} \right)^{-5/7} \left(\frac{\dot{M}}{\dot{M}_{\text{Edd}}} \right)^{-3/7} R_6^{18/7} \quad (6.1)$$

where B_9 is the surface field in 10^9 Gauss, M is the mass of the star, \dot{M} is the rate of accretion and R_6 is the radius of the star in units of 10 km. Therefore, the wind phase has two distinct sub-phases, namely - the propeller phase and the

phase of actual wind accretion. It must be noted here that the duration of these two sub-phases vary widely from system to system and the phase of actual wind accretion may not at all be realized in some cases. For models based on an initial crustal field configuration, the phase of wind accretion and the subsequent phase of Roche contact play the all-important role.

3. The Roche-contact Phase - When the companion of the neutron star fills its Roche-lobe a phase of heavy mass transfer ($\dot{M} \sim \dot{M}_{\text{Edd}}$) ensues. Though short-lived in case of HMXBs ($\sim 10^4$ years), this phase can last as long as 10^9 years for LMXBs. Consequently, this phase is very important for field evolution in LMXBs.

The nature of the binary evolution is well studied in the case of the LMXBs where the mass transfer proceeds in a controlled manner. The same is true for the wind phase in the HMXBs. But the exact nature of mass transfer in the common-envelope phase, due to Roche-lobe overflow, has not been studied in any detail yet. Still, due to the short-lived nature this phase does not affect the field evolution significantly and therefore the lack of precise knowledge does not affect our calculations much. On the other hand, not much attention has been paid to the evolution of the intermediate systems with companion masses in the range $\sim 2 - 5 M_{\odot}$. They are most likely to have an intermediate nature in that the wind phase is prolonged and the accretion rates are similar to those in the wind phase of low-mass systems, whereas, the Roche-contact phase is perhaps similar to that in HMXBs. In either of the phases it would be difficult to observe these systems, owing to the low luminosity in the wind phase and due to the short-lived nature of the Roche-contact phase. Moreover, in HMXBs and intermediate mass binaries Roche-contact would usually lead to a common-envelope evolution. In this phase the neutron star is engulfed by the common envelope and the X-ray flux is hidden from the view. So far no intermediate-mass system has been observed in the X-ray phase. As for the pulsars processed in them, there are perhaps three examples PSR B0655+64, PSR J2145-0750 and PSR J1022+1001 (Camilo et al. 1996). But because of the uncertainties surrounding their mass transfer history we exclude this kind of binaries from the present discussion.

6.4 computations

Using the methodology developed in chapter [5] we solve equation [5.16] following the mass-transfer history on neutron stars in high-mass and low-mass binary systems. For

the case of isolated pulsars we solve the following equation,

$$\frac{\partial \vec{B}}{\partial t} = -\frac{c^2}{4\pi} \vec{\nabla} \times \left(\frac{1}{\sigma} \times \vec{\nabla} \times \vec{B} \right). \quad (6.2)$$

For all of the above cases we shall assume an initial crustal current configuration (the kind that has been used in chapter [5]).

6.4.1 binary parameters

The binary evolution parameters for the LMXBs and the HMXBs used by us are as follows (Verbunt 1990; Bhattacharya & van den Heuvel 1991; van den Heuvel 1992; Bitzaraki & van den Heuvel 1995; King et al. 1995) -

1. Low Mass X-ray Binaries -

- (a) Isolated phase - Though binaries with narrow orbits may not have too-long-lived a phase of completely detached evolution, long period binaries (like the progenitor system of PSR 0820+02 with ~ 250 day orbital period (Verbunt & van den Heuvel 1995)) may spend longer than 10^9 years before contact is established. In general, the isolated phase lasts between $10^8 - 10^9$ years.
- (b) Wind phase - This phase again lasts for about $10^8 - 10^9$ years with attendant rates of accretion ranging from about $10^{-15} M_{\odot} \text{ yr}^{-1}$ to $10^{-12} M_{\odot} \text{ yr}^{-1}$.
- (c) Roche-contact phase - In this phase, the mass transfer rate could be as high as the Eddington rate ($10^{-8} M_{\odot} \text{ yr}^{-1}$ for a $1.4 M_{\odot}$ neutron star), lasting for $\lesssim 10^8$ years. But there has been recent indications that the low-mass binaries may even spend $\sim 10^{10}$ years in the Roche-contact phase with a sub-Eddington accretion rate (Hansen & Phinney 1997). For wide binaries, however, the contact phase may last as little as 10^7 years. We have investigated the cases with accretion rates of $10^{-10} M_{\odot} \text{ yr}^{-1}$ and $10^{-9} M_{\odot} \text{ yr}^{-1}$. With a higher accretion rate the material movement is faster and therefore the 'freezing-in' takes place earlier (see figure [5.10]). Moreover, the equation [2.13], used by us to find the crustal temperature for a given rate of accretion, gives temperatures that are too high for accretion rates above $10^{-10} M_{\odot} \text{ yr}^{-1}$. The neutrino cooling is likely to prevent the temperature from reaching such large values and therefore for high rates of accretion probably the crustal temperature would reach a maximum saturation value. In our calculations we assume that the temperature that could be attained by accretion-induced heating is $\sim 10^{8.5}$ K for an accretion rate of $10^{-9} M_{\odot} \text{ yr}^{-1}$. For reasons noted in the previous chapter we are unable to make detailed calculations for $\dot{M} \gtrsim 10^{-9} M_{\odot} \text{ yr}^{-1}$.

2. High Mass X-ray Binaries -

- (a) Isolated phase - This phase is short in binaries with a massive companion and may last as little as ten thousand years.
- (b) Wind phase - This phase is also relatively short (compared to the low-mass systems), lasting not more than 10^7 years (equivalent to the main-sequence life time of the massive star), with accretion rates ranging from $10^{-14} M_{\odot} \text{ yr}^{-1}$ to $10^{-10} M_{\odot} \text{ yr}^{-1}$.
- (c) Roche-contact phase - A rapid phase of Roche-lobe overflow follows the wind phase. The rate of mass shedding by the companion could be as high as one tenth of a solar mass per year, of which a tiny fraction is actually accreted by the neutron star (the maximum rate of acceptance being presumably equal to the Eddington rate). The duration of this phase is $\lesssim 10^4$ years.

We must mention here about the Globular Cluster binaries though we have not performed any explicit calculations for such systems. The duration and the rates of mass accretion vary widely depending on how the mass transfer phase ends in such binaries. The mass transfer may end through binary disruption, by the neutron star spiraling in or through a slow turn off.

6.4.2 thermal behaviour

The thermal behaviour of isolated pulsars and of those accreting material from their binary companions differs from each other significantly (for details see section[2.3]). Since crustal temperature is one of the major factors controlling field evolution we need to consider the thermal behaviour with some care. For a neutron star that is a member of a binary, the thermal behaviour will be similar to that of an isolated neutron star before the advent of actual mass transfer. Therefore through the isolated and the propeller phase the neutron star cools like an isolated one. In particular, in the low-mass systems the duration of the isolated phase and the propeller phase could be quite long and therefore is rather important in affecting the subsequent evolution of the surface field. We have shown in the previous chapter that a phase of field evolution in the isolated phase modifies the subsequent evolution considerably. Therefore, it is necessary to take into account the proper cooling history of the neutron star prior to the establishment of contact with its binary companion. As mentioned before, we investigate both the cases - with standard and accelerated cooling. Of course, the isolated phase itself is of importance only in case of an initial crustal field configuration, the topic of our discus-

sion in the present chapter. For initial currents supported in the superconducting core, the crustal physics of the star is mostly irrelevant as the field has not yet been expelled to the crust. When, in the course of binary evolution, the neutron star actually starts to accrete mass - the thermal behaviour changes from that characteristic of an isolated phase. The crustal temperature then settles down to a steady value determined by the accretion rate as given in equation [2.13].

6.4.3 crustal physics

We have seen in chapter [5] that the field evolution stops as the field *freezes in* when about 10% of the original crustal mass is accreted. This happens due to the fact that by then the current loops reach the regions of extremely high, electrical conductivity. The mass of the crust of a $1.4 M_{\odot}$ neutron star, with our adopted equation of state, is $\sim 0.044 M_{\odot}$. Therefore, in the present investigation we stop our evolutionary code when $\sim 0.01 - 0.04 M_{\odot}$ is accreted. From our results (presented in section [6.5]) it is evident that the field evidently shows signs of 'freezing in' when we stop our calculation. Of course, as we have mentioned earlier, to achieve millisecond period about 0.1 solar mass requires to be accreted. But once the field attains its 'frozen-in' value subsequent accretion does not affect it in any way. Therefore, the final spin-period is determined by this value of the surface field in accordance with equation [6.1].

6.5 results and discussions

6.5.1 solitary neutron stars

Figure [6.2] shows the evolution of the surface field in an isolated neutron star due to pure ohmic decay, for different densities at which the initial current distribution is concentrated. We have seen it before too, that the lower the density of current concentration the more rapid is the decay of the field. This figure refers to a situation where the impurity strength has been assumed to be zero. In figure [6.3] we plot similar curves for the evolution of the surface field with an assumed $Q = 0.05$. In this case the final field values are too small to be consistent with the indication from the statistical analyses. We find that the maximum value of Q that can be allowed is about 0.01 if allow for a maximum decay by two orders of magnitude within solitary pulsar active lifetime. In figures [6.4] and [6.5] we plot similar curves assuming a fast cooling process for the thermal behaviour of the star. It is seen that the decay is evidently much less than in the case of the standard cooling. But even in this case the maximum

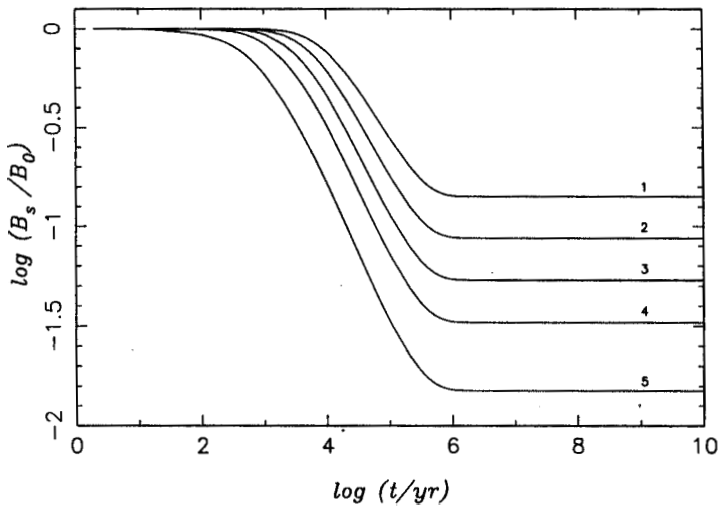


Figure 6.2: The evolution of the surface magnetic field due to pure diffusion. Curves 1 to 5 correspond to densities of 10^{13} , $10^{12.5}$, 10^{12} , $10^{11.5}$, 10^{11} g cm^{-3} respectively, at which the g-profiles are centred. All curves correspond to $Q = 0$. Standard cooling has been assumed here.

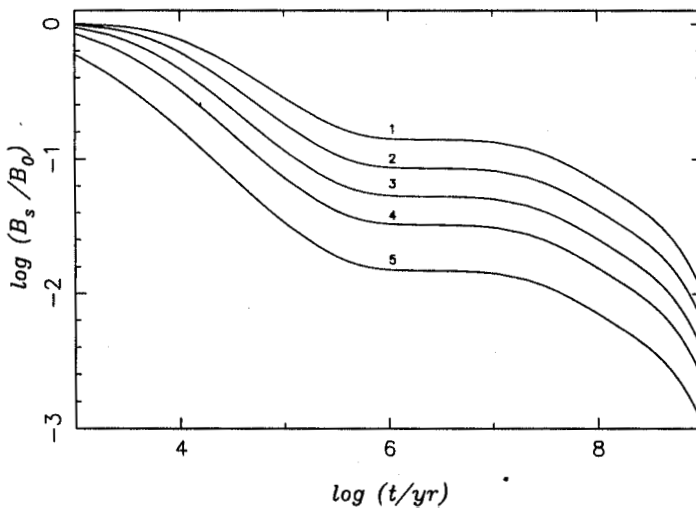


Figure 6.3: Same as figure [6.2] but with $Q = 0.05$.

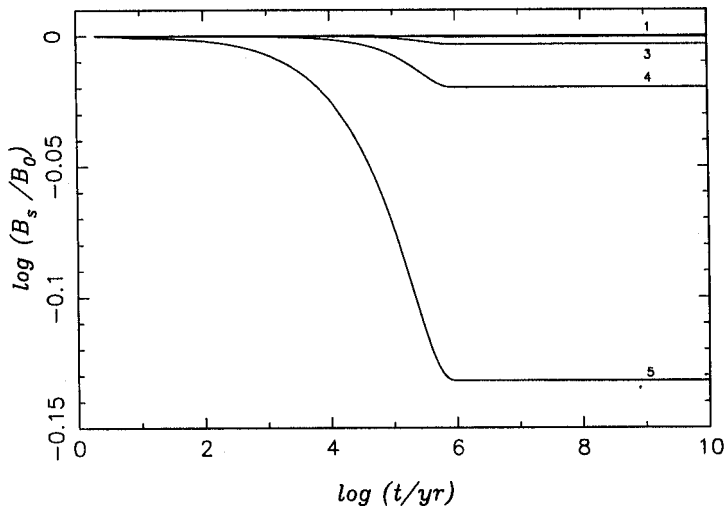


Figure 6.4: Same as figure [6.2] but with accelerated cooling assumed.

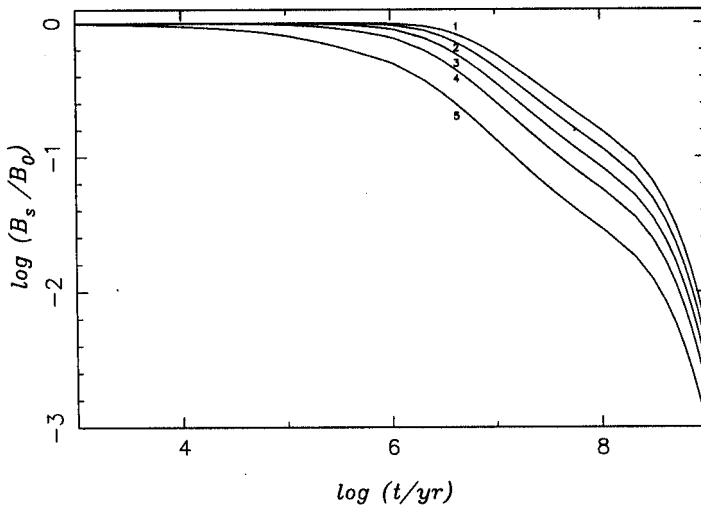


Figure 6.5: Same as figure [6.4] but with $Q = 0.1$.

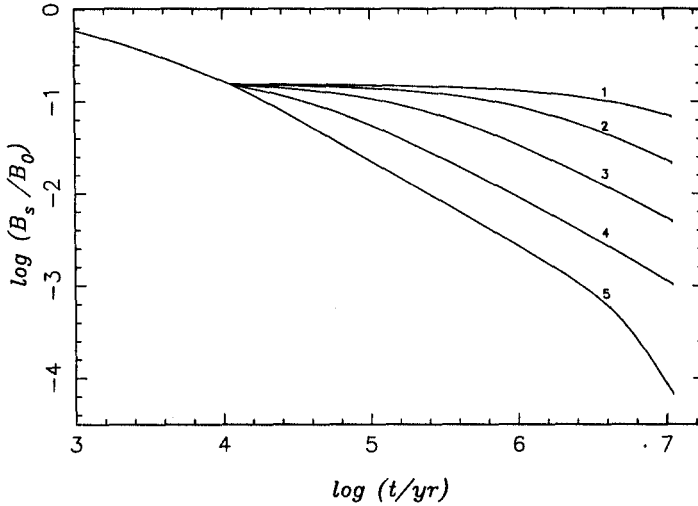


Figure 6.6: Evolution of the surface magnetic field in HMXBs for four values of wind accretion rate with slow cooling behaviour in the isolated phase. The curves 1 to 5 correspond to $M = 10^{-14}, 10^{-13}, 10^{-12}, 10^{-11}, 10^{-10} M_{\odot} \text{ yr}^{-1}$. All curves correspond to an initial current configuration centred at $p = 10^{11} \text{ g cm}^{-3}$, an accretion rate of $M = 10^{-8} M_{\odot} \text{ yr}^{-1}$ in the Roche-contact phase and $Q = 0.0$.

Q value permissible is about 0.05. This we shall see later that is in contradiction with the requirements of a spin-down induced flux expulsion model.

6.5.2 high mass binaries

Figures [6.6] to [6.15] show the evolution of the surface field in the HMXBs; for different values of the density at which the initial current profile is centred at. Figures [6.6] to [6.10] correspond to computations with standard cooling in the isolated phase, whereas figures [6.11] to [6.15] correspond to calculations with an accelerated cooling in the isolated phase. For all of these cases we have assumed a Roche-contact phase lasting for 10^4 years with a uniform rate of accretion of $10^{-8} M_{\odot} \text{ yr}^{-1}$. Since the Roche-contact phase is extremely short-lived, the actual field decay takes place in the wind phase. In fact, the decay attained in the Roche-contact phase is insignificant and is not quite visible in figures [6.6] to [6.15]. In figure [6.16] we show an expanded version of figure [6.6] highlighting this final phase.

From these figures it is evident that if the initial current distribution is located at high

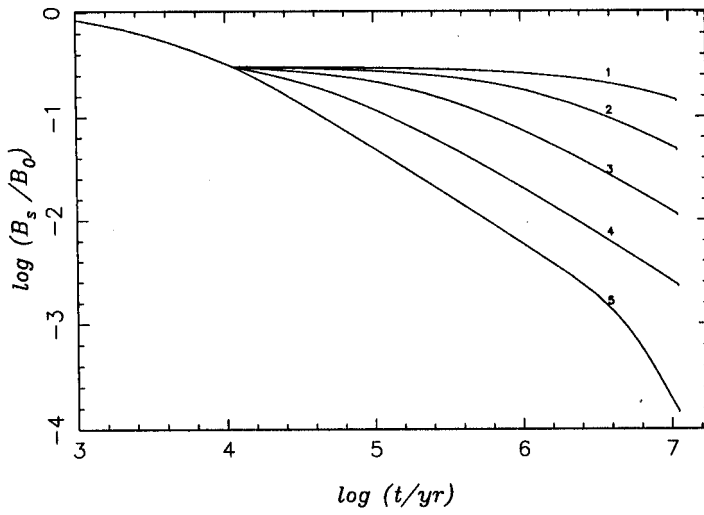


Figure 6.7: Same as figure [6.6] with an initial current configuration centred at $\rho = 10^{11.5} \text{g cm}^{-3}$.

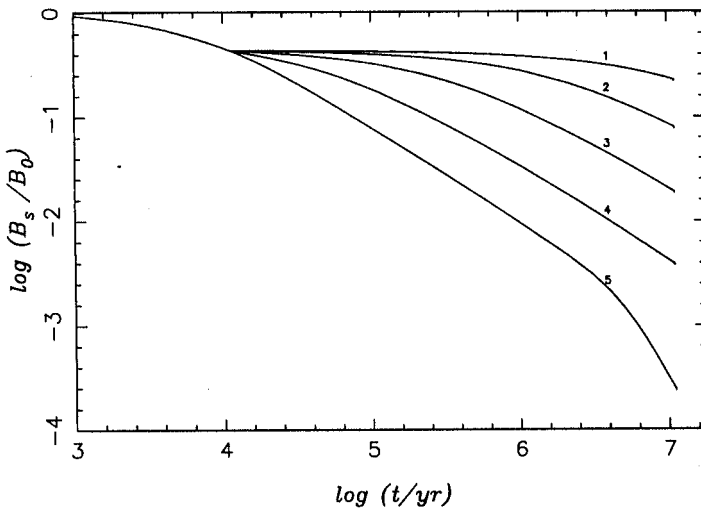


Figure 6.8: Same as figure [6.6] with an initial current configuration centred at $\rho = 10^{12} \text{g cm}^{-3}$.

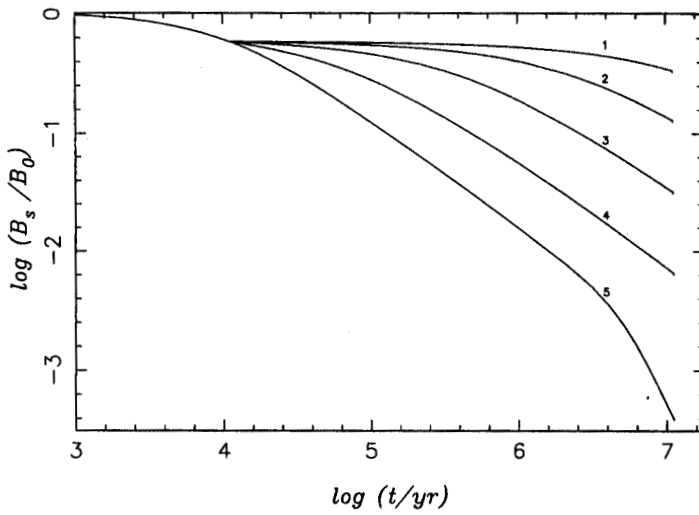


Figure 6.9: Same as figure [6.6] with an initial current configuration centred at $\rho = 10^{12.5} \text{g cm}^{-3}$.

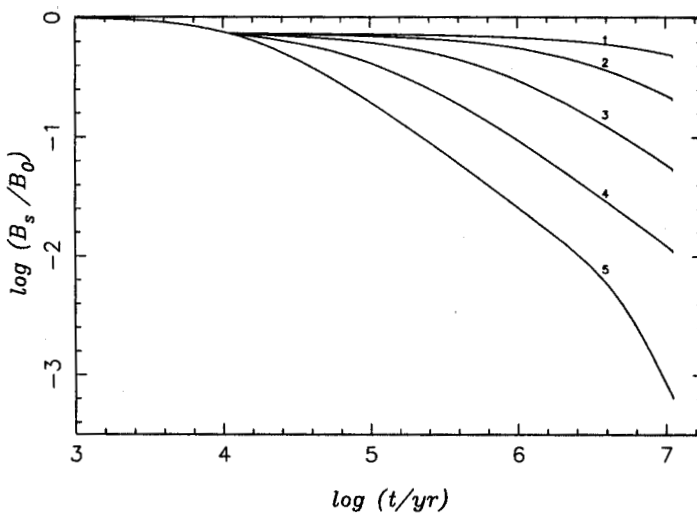


Figure 6.10: Same as figure [6.6] with an initial current configuration centred at $\rho = 10^{13} \text{g cm}^{-3}$.

densities the objects from high-mass systems will retain fairly large final fields. Even for low density current distributions, if the duration of the wind phase is not too long - again high-field objects are produced. We expect these objects to show up as recycled pulsars with relatively high fields and long periods like PSR B1913+16 or PSR B1534+12. On the other hand, if the wind phase lasts for about 10^7 years, it is possible to obtain a significant field decay for higher rates of accretion in that phase. But as the total mass and hence the total angular momentum accreted is not sufficient to spin the star up to very short periods, these systems probably would not produce millisecond pulsars. In other words these so-called 'recycled' pulsars would have small magnetic fields with relatively long spin-periods and therefore may not at all be active as pulsars. We make an estimate of the actual spin-up for objects processed in high-mass systems to check this fact.

The spin-up of a neutron star, in a binary system, is caused by the angular momentum brought in by the accreted matter. In magnetospheric accretion matter accretes with angular momentum specific to the Alfvén radius. Therefore, the total angular momentum brought in by accretion is

$$J_{\text{accreted}} = \delta M R_A V_A \quad (6.3)$$

where δM is the total mass accreted. R_A and V_A are the Alfvén radius and Keplerian velocity at that radius given by equations [4.9] and [4.5]. The final period of the neutron star then is

$$P_{\text{final}} = 2\pi \frac{I_{\text{ns}}}{J_{\text{accreted}}}, \quad (6.4)$$

where I_{ns} is the moment of inertia of the neutron star. In figure [6.18] we have indicated the possible location of the 'recycled' pulsars originating in HMXBs. We find that for sufficiently low field strengths ($B \lesssim 10^9$ Gauss) the recycled pulsars indeed will be beyond the death line. And active pulsars with slightly higher fields will lie very close to the death line. Comparing this figure with the field-period diagram of the observed pulsars (figure [6.17]) one does find pulsars like PSR 0655+64 to fall in this category. The cases of high-field pulsars well above death line are also quite evident from this figure.

It should also be noted here that even though the nature of field evolution is very different in the isolated phase for standard and accelerated cooling, the final surface field values at the end of the wind phase are not very different. This is due to the fact that the nature of the field evolution is significantly influenced by previous history. We have

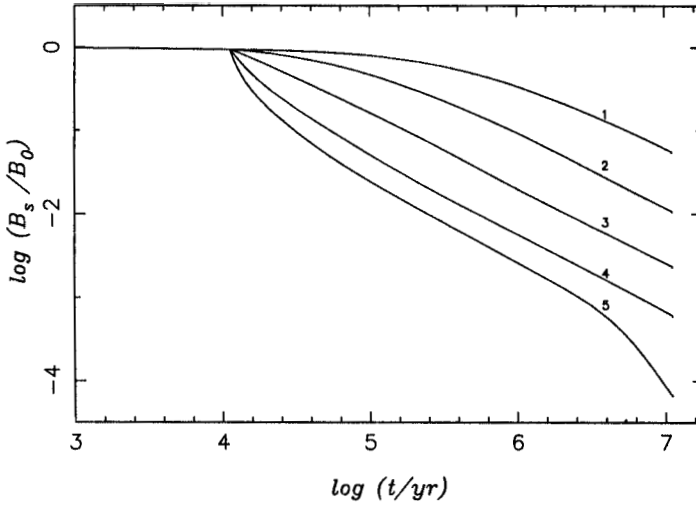


Figure 6.11: Evolution of the surface magnetic field in HMXBs for four values of wind accretion rate with accelerated cooling behaviour in the isolated phase. The curves 1 to 5 correspond to $M = 10^{-14}, 10^{-13}, 10^{-12}, 10^{-11}, 10^{-10} M_{\odot} \text{ yr}^{-1}$. All curves correspond to an initial current configuration centred at $\rho = 10^{11} \text{ g cm}^{-3}$, an accretion rate of $M = 10^{-8} M_{\odot} \text{ yr}^{-1}$ in the Roche-contact phase and $Q = 0.0$.

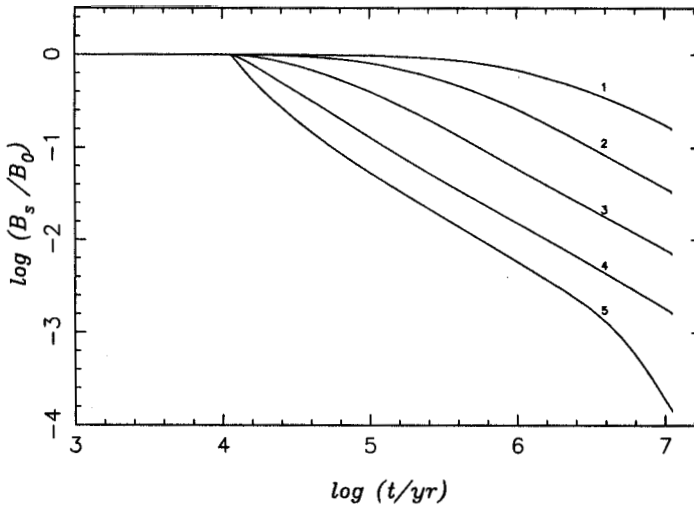


Figure 6.12: Same as figure [6.11] with an initial current configuration centred at $\rho = 10^{11.5} \text{ g cm}^{-3}$.

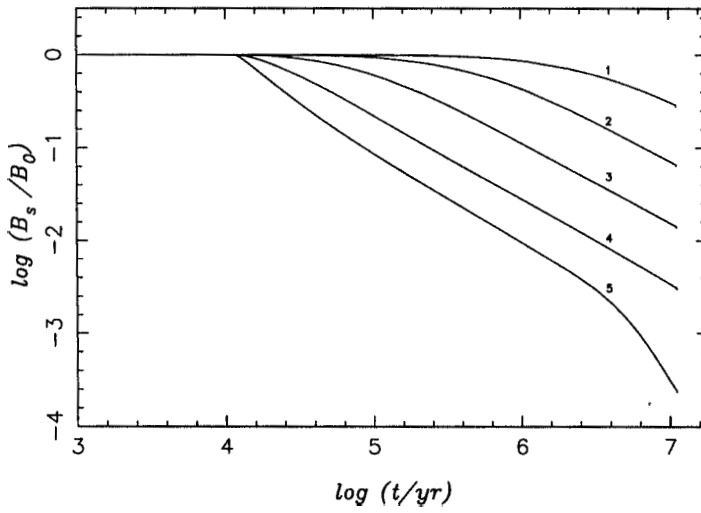


Figure 6.13: Same as figure [6.11] with an initial current configuration centred at $\rho = 10^{12} \text{g cm}^{-3}$.

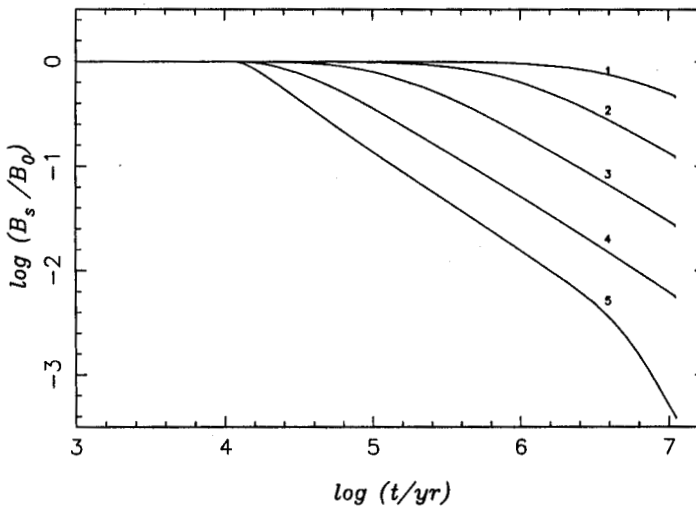


Figure 6.14: Same as figure [6.11] with an initial current configuration centred at $\rho = 10^{12.5} \text{g cm}^{-3}$.

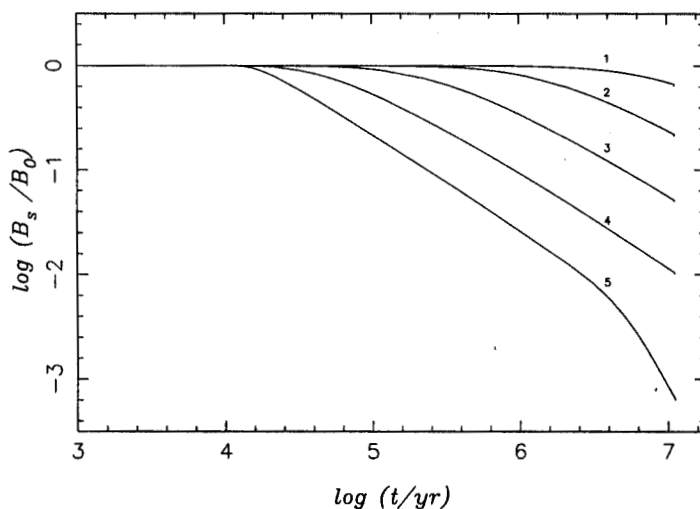


Figure 6.15: Same as figure [6.11] with an initial current configuration centred at $\rho = 10^{13} \text{g cm}^{-3}$.

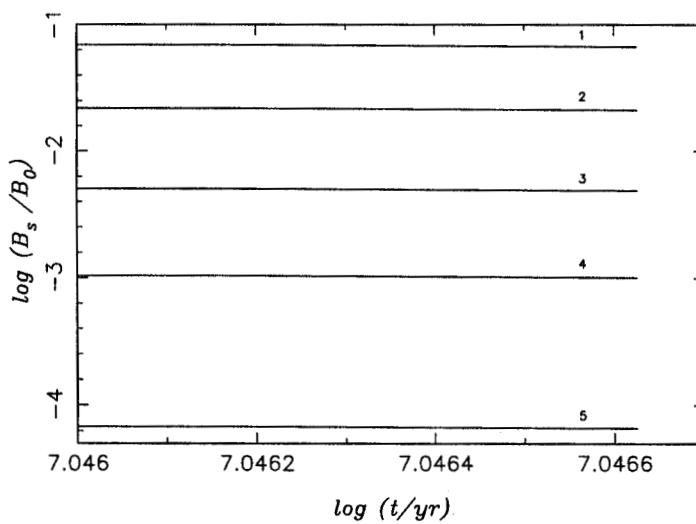


Figure 6.16: Same as figure [6.6] with the final Roche-contact phase expanded.

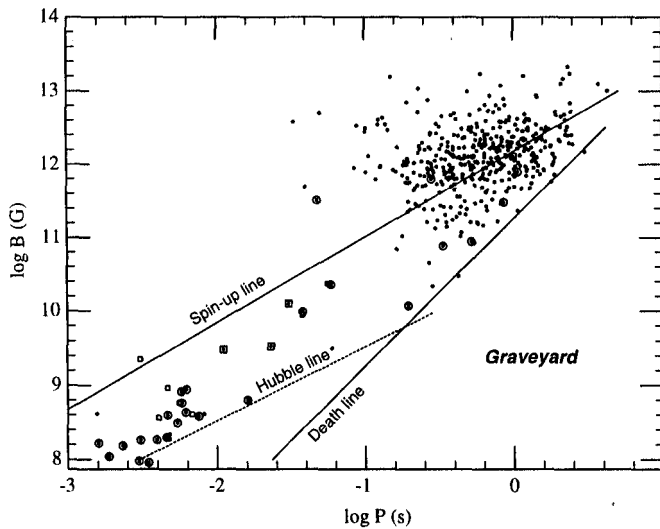


Figure 6.17: The measured periods and the derived surface dipole field of observed pulsars. The filled circles and the filled circles within open circles correspond isolated and binary pulsars in the galactic disc. The open squares and the filled circles within open squares correspond to isolated and binary pulsars in globular clusters. On the right hand side of the death line pulsar activity stops. The spin-up line correspond to the minimum spin-period that can be achieved through binary recycling assuming an Eddington accretion rate. The Hubble line correspond to the characteristic age of the pulsars equal to the age of the universe.

already seen in chapter [5] (see figure [5.21]) that subsequent decay is slowed down in a system with a history of prior field decay than in systems without any. The decay in the isolated phase is less for accelerated cooling, but in the subsequent wind accretion phase the field decays more rapidly in such systems than in those starting with standard cooling. We shall see a more dramatic manifestation of this fact in LMXBs where the duration of the isolated phase is much longer.

6.5.3 low mass binaries

Figures [6.19] to [6.30] show the evolution of the surface field in LMXBs. In figures [6.19] and [6.20] we plot the complete evolution of the surface field for two values of the accretion rate in the wind phase and five values of the density at which currents are initially concentrated, assuming standard cooling in the isolated phase. But in these figures, the wind and Roche-contact phases are not clearly distinguishable. Therefore we have plotted the expanded versions of these figures to highlight the individual phases.

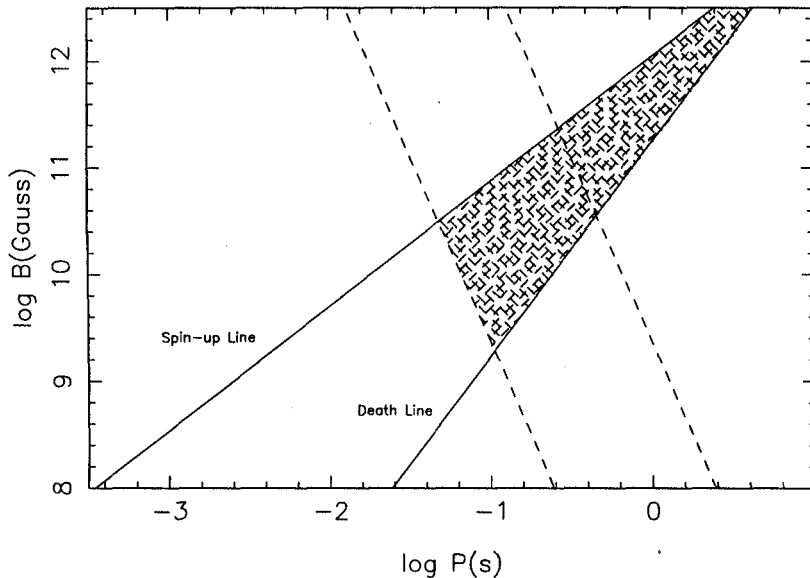


Figure 6.18: The probable location of HMXB progenies in the field-period diagram. The dashed lines correspond to the maximum spin-up achievable, the upper and the lower lines being for assumed accreted masses of 10^{-4} and $10^{-3} M_{\odot}$. The recycled pulsars from HMXBs are expected to lie within the hatched region.

Figures [6.21] and [6.22] are for the wind-phase whereas figures [6.23] and [6.24] are for the Roche-contact phase corresponding to those plots. In figures [6.27] to [6.30] we plot the corresponding figures with an accelerated cooling in the isolated phase.

It is seen from these figures that the surface field drops by half to one order of magnitude in the wind phase of the binary evolution. When the system is in contact through Roche-lobe overflow the field decay depends very much on the rate of accretion. A difference in the accretion rate in this phase shows up as a difference in the final value of the surface field, which freezes at a higher value for higher rates of accretion. The total decay in the Roche-contact phase may be as large as two to three orders of magnitude with respect to the magnitude of the field at the end of the wind phase.

We have mentioned before that the phase of wind accretion may not be realized in some of the cases at all. In figures [6.31] to [6.34] we have plotted the evolution of the surface field for such cases, both for the standard and the accelerated cooling. We find that the final field strengths achieved without a phase of wind accretion is not very different from the cases where such a phase does exist. This again is indicative of the fact that a prior phase of field decay slows down the decay in the subsequent phase.

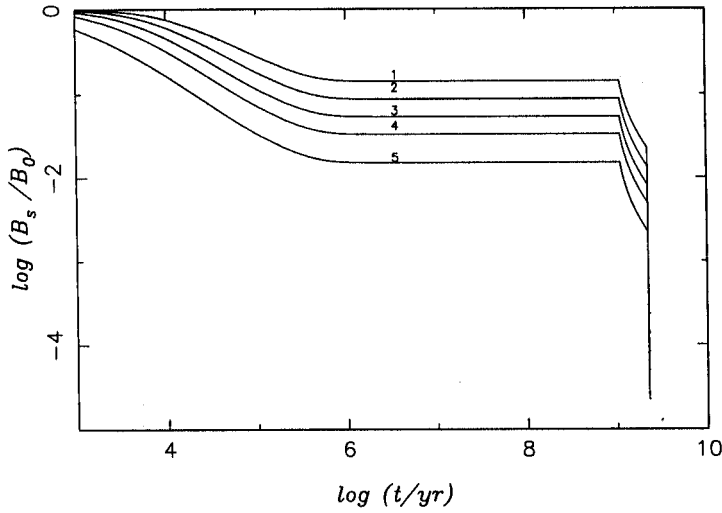


Figure 6.19: Evolution of the surface magnetic field in LMXBs with an wind accretion rate of $M = 10^{-16} M_{\odot} \text{ yr}^{-1}$, accretion rates of $M = 10^{-10}, 10^{-9} M_{\odot} \text{ yr}^{-1}$ in the Roche-contact phase. Curves 1 to 5 correspond to initial current configuration centred at $\rho = 10^{11}, 10^{11.5}, 10^{12}, 10^{12.5}, 10^{13} \text{ g cm}^{-3}$. All curves correspond to $Q = 0.0$. A standard cooling has been assumed for the isolated phase here.

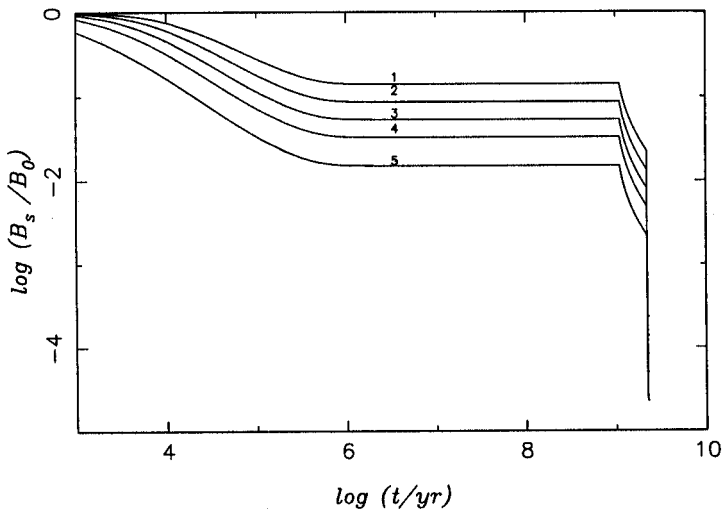


Figure 6.20: Same as figure [6.19] but with an wind accretion rate of $M = 10^{-14} M_{\odot} \text{ yr}^{-1}$.

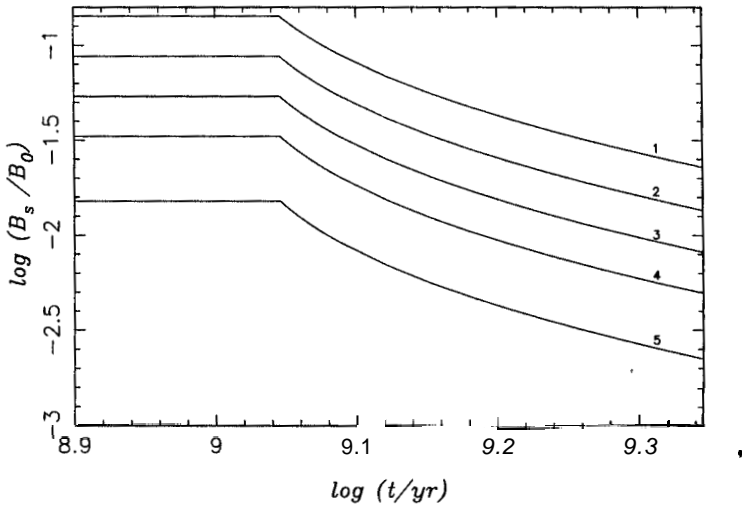


Figure 6.21: Same as figure [6.19] with the wind phase expanded.

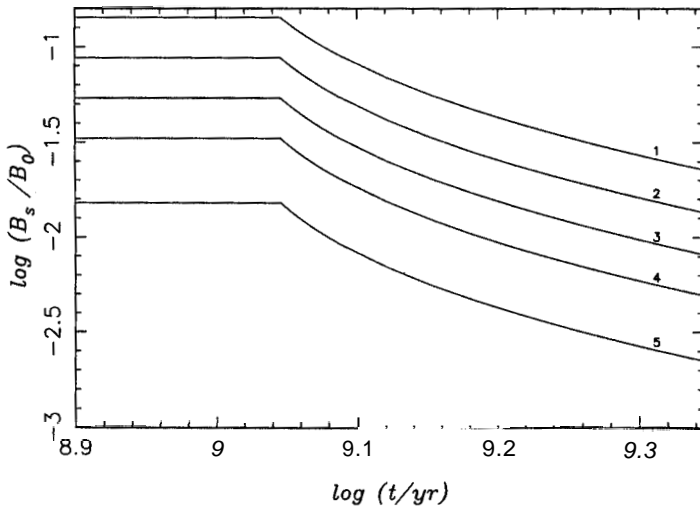


Figure 6.22: Same as figure [6.20] with the wind phase expanded.

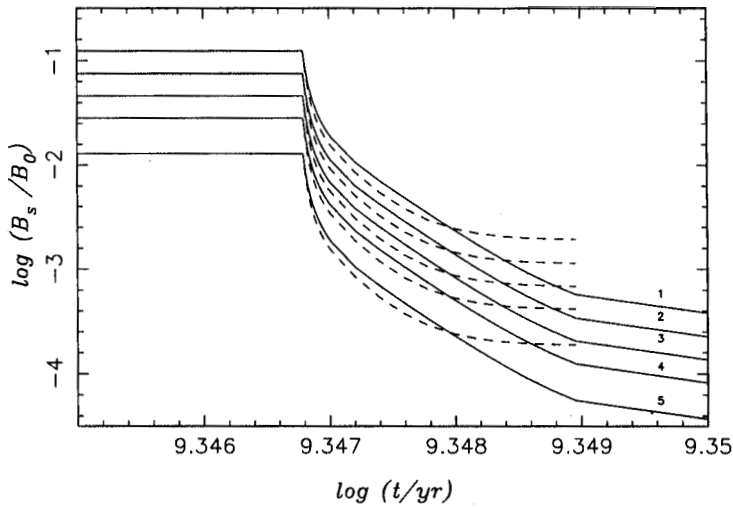


Figure 6.23: Roche-contact phase of figure [6.19] expanded. The solid and the dotted lines correspond to the accretion rates of $10^{-10} M_{\odot} \text{ yr}^{-1}$ and $10^{-9} M_{\odot} \text{ yr}^{-1}$ in the Roche-contact phase corresponding to each initial current concentration density.

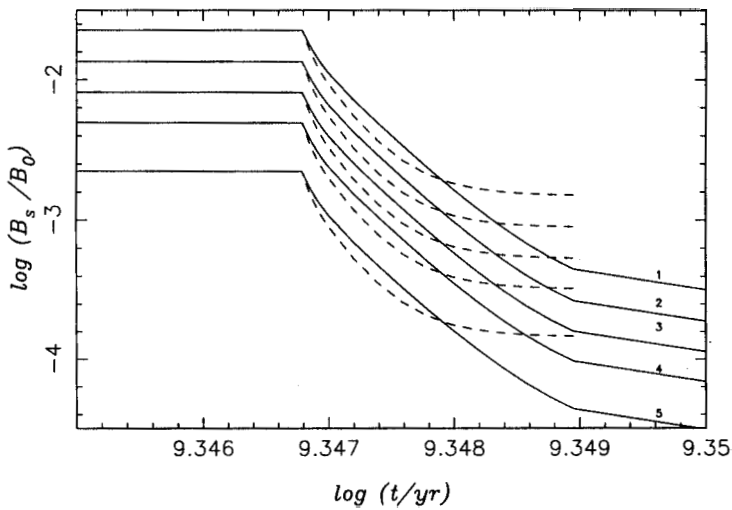


Figure 6.24: Roche-contact phase of figure [6.20] expanded. The solid and the dotted lines correspond to the accretion rates of $10^{-10} M_{\odot} \text{ yr}^{-1}$ and $10^{-9} M_{\odot} \text{ yr}^{-1}$ in the Roche-contact phase corresponding to each initial current concentration density.

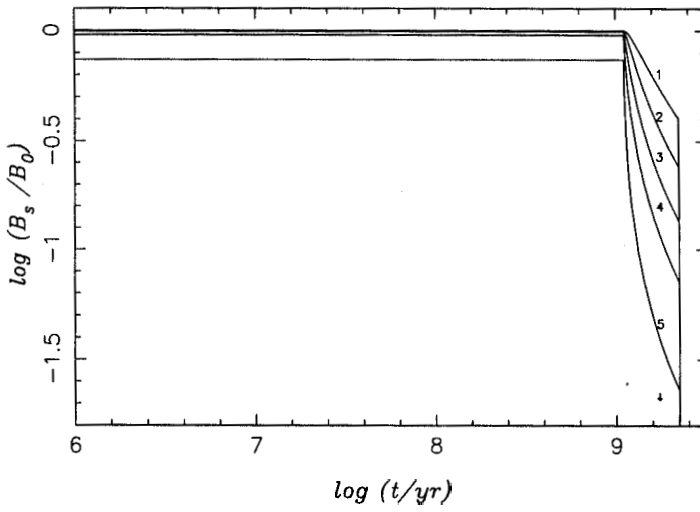


Figure 6.25: Same as figure [6.19] but with an accelerated cooling in the isolated phase.

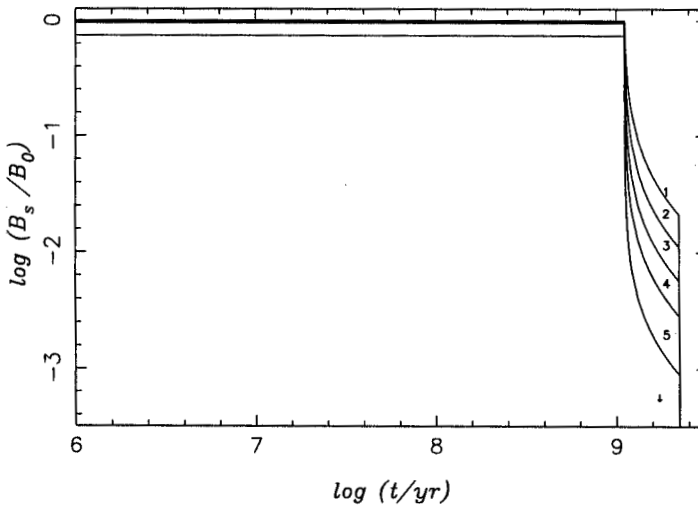


Figure 6.26: Same as figure [6.20] but with an accelerated cooling in the isolated phase.

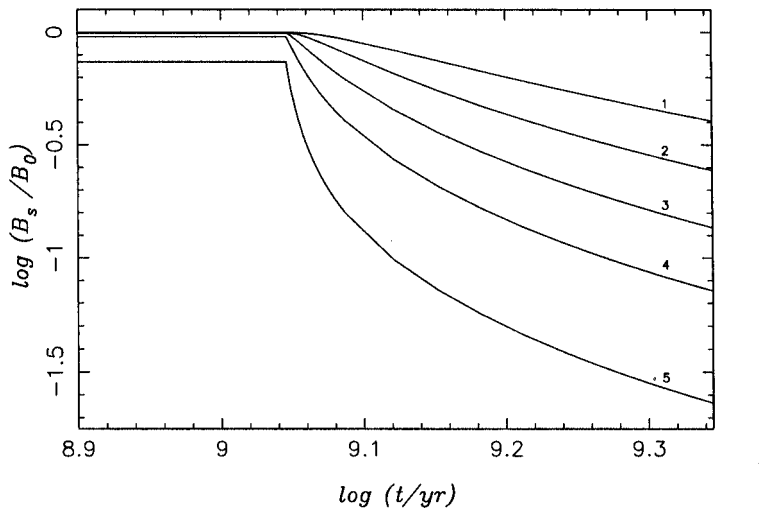


Figure 6.27: The wind accretion phase of figure [6.25] expanded.

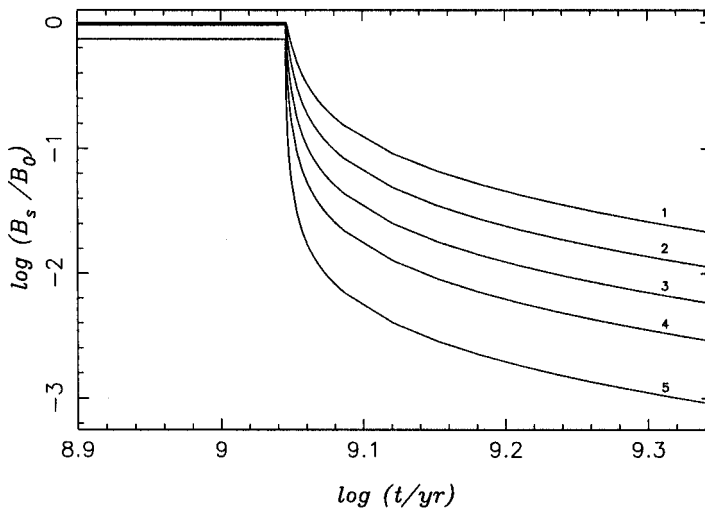


Figure 6.28: The wind accretion phase of figure [6.26] expanded.

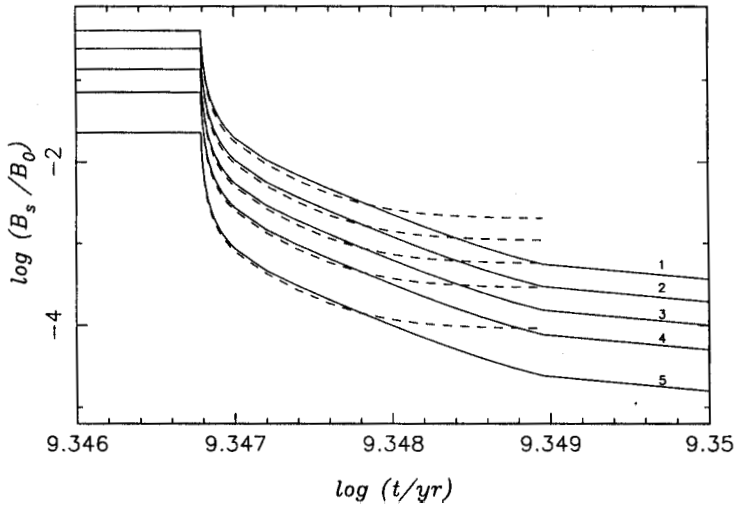


Figure 6.29: Roche contact phase of figure [6.25] expanded. The solid and the dotted lines correspond to the accretion rates of $10^{-10} M_{\odot} \text{ yr}^{-1}$ and $10^{-9} M_{\odot} \text{ yr}^{-1}$ in the Roche-contact phase corresponding to each initial current concentration density.

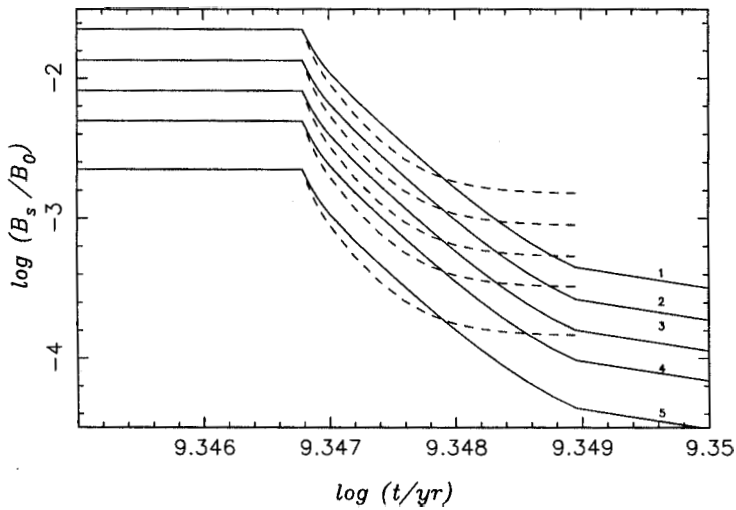


Figure 6.30: Roche contact phase of figure [6.26] expanded. The solid and the dotted lines correspond to the accretion rates of $10^{-10} M_{\odot} \text{ yr}^{-1}$ and $10^{-9} M_{\odot} \text{ yr}^{-1}$ in the Roche-contact phase corresponding to each initial current concentration density.

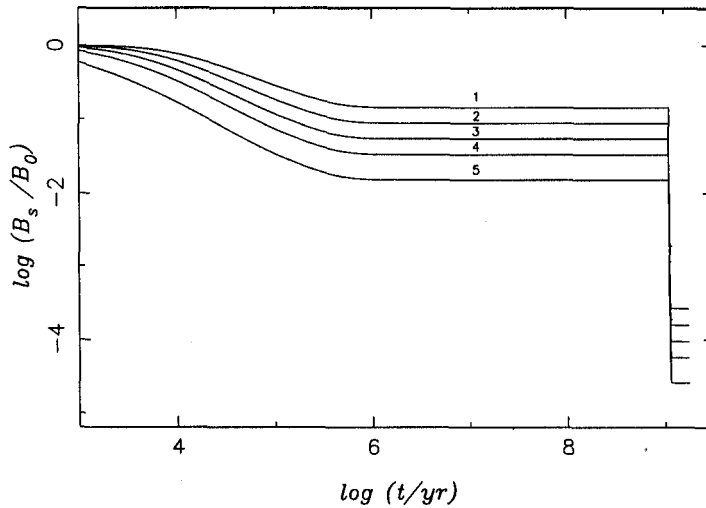


Figure 6.31: Evolution of the surface magnetic field in LMXBs without a phase of wind accretion and accretion rates of $\dot{M} = 10^{-10}, 10^{-9} M_{\odot} \text{ yr}^{-1}$ in the Roche-contact phase. Curves 1 to 5 correspond to initial current configuration centred at $\rho = 10^{11}, 10^{11.5}, 10^{12}, 10^{12.5}, 10^{13} \text{ g cm}^{-3}$. All curves correspond to $Q = 0.0$. A standard cooling has been assumed for the isolated phase here.

And therefore the final result from both the cases become similar

There are several interesting points to note here. Figures [6.23], [6.24],[6.29], and [6.30] shows that for higher values of accretion rate in the Roche-contact phase the final field values are higher. We have not explored the case of accretion with an Eddington rate in this phase. From the trends observed in our calculation it is evident that with such high rate of accretion the final field value may remain fairly large. Under such circumstances it will be possible to have 'recycled' pulsars of high surface magnetic field (and therefore long spin-period) from low mass binaries and pulsars like PSR 0820+02 will fit in with the general scenario quite well. Then, of course, we do find significant amount of field decay with lower rates of accretion in the Roche-contact phase. Such low surface fields combined with the provision of maximal spin-up would then produce millisecond pulsars.

Figures [6.6] to [6.30] then indicate that the model of field evolution assuming an initial crustal field configuration is quite consistent with the present scenario of field evolution. The LMXBs will produce high-field, long-period pulsars in addition to the

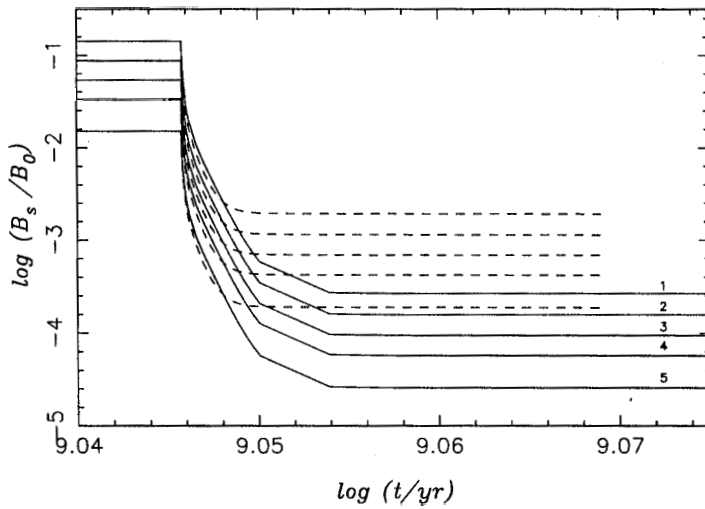


Figure 6.32: The Roche-contact phase of figure [6.31] expanded. The solid and the dotted lines correspond to the accretion rates of $10^{-10} M_{\odot} \text{ yr}^{-1}$ and $10^{-9} M_{\odot} \text{ yr}^{-1}$ in the Roche-contact phase corresponding to each initial current concentration density.

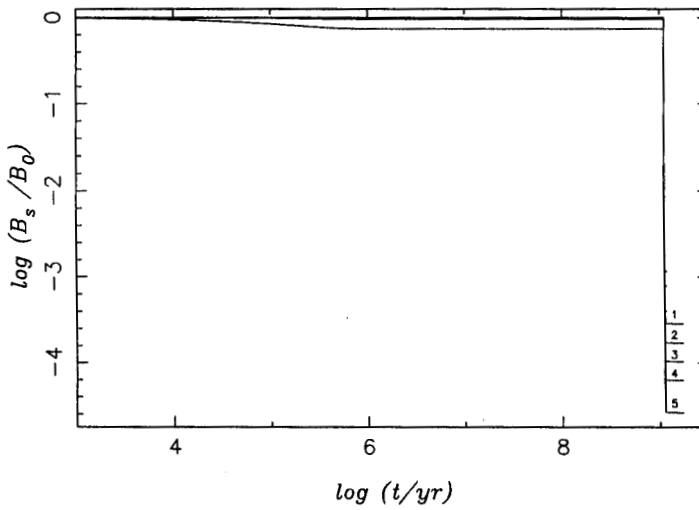


Figure 6.33: Same as figure [6.31] with accelerated cooling assumed for the isolated phase.

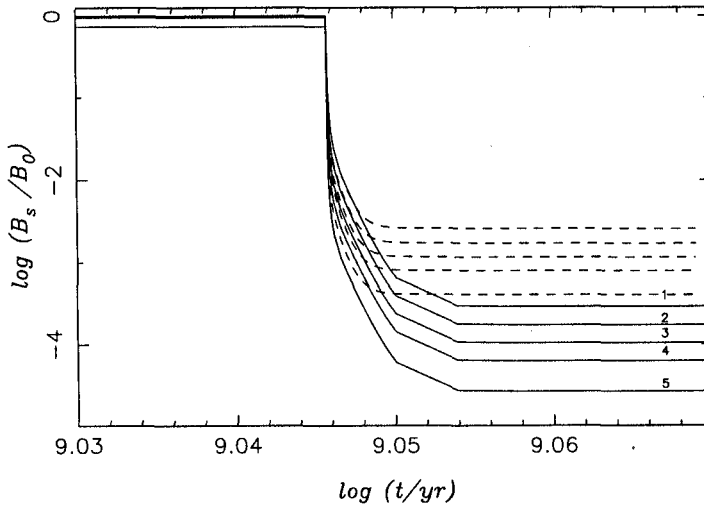


Figure 6.34: Same as figure [6.32] with accelerated cooling assumed for the isolated phase.

expected crop of millisecond pulsars. Whereas the only kind of recycled pulsars that are expected from the HMXBs would be of the relatively high-field, long-period variety.

In the course of our investigations in this chapter we have seen that there is a positive correlation between the rate of accretion with that of the final field strength, namely, the higher the rate of accretion the higher is the final field. There has already been a mention of such a correlation in connection with the Z and Atoll sources (Hasinger & van der Klis 1989). It was suggested that the difference between these two classes of sources in regard to their fluctuation spectra is not only due to a difference in the accretion rate but also due to a difference in the magnetic field. And there has been indication from the study of the radiation spectra of these sources that the accretion rate and the magnetic field strength are positively correlated. Recently, Psaltis & Lamb (1997) on the basis of LMXB spectra and White & Zhang (1997) on the basis of the properties of the kilohertz QPOs have indicated the existence of such a correlation. Consider figure [6.35] - the top and the middle panels are taken from van den Heuvel & Bitzaraki (1995) and the bottom panel is made using the data from Verbunt & van den Heuvel (1995). The middle panel shows the variation of the magnetic field with the orbital period for some of the low mass binary pulsars whereas the bottom panel shows the rate of mass accretion with the orbital period in low-mass X-ray binary systems.

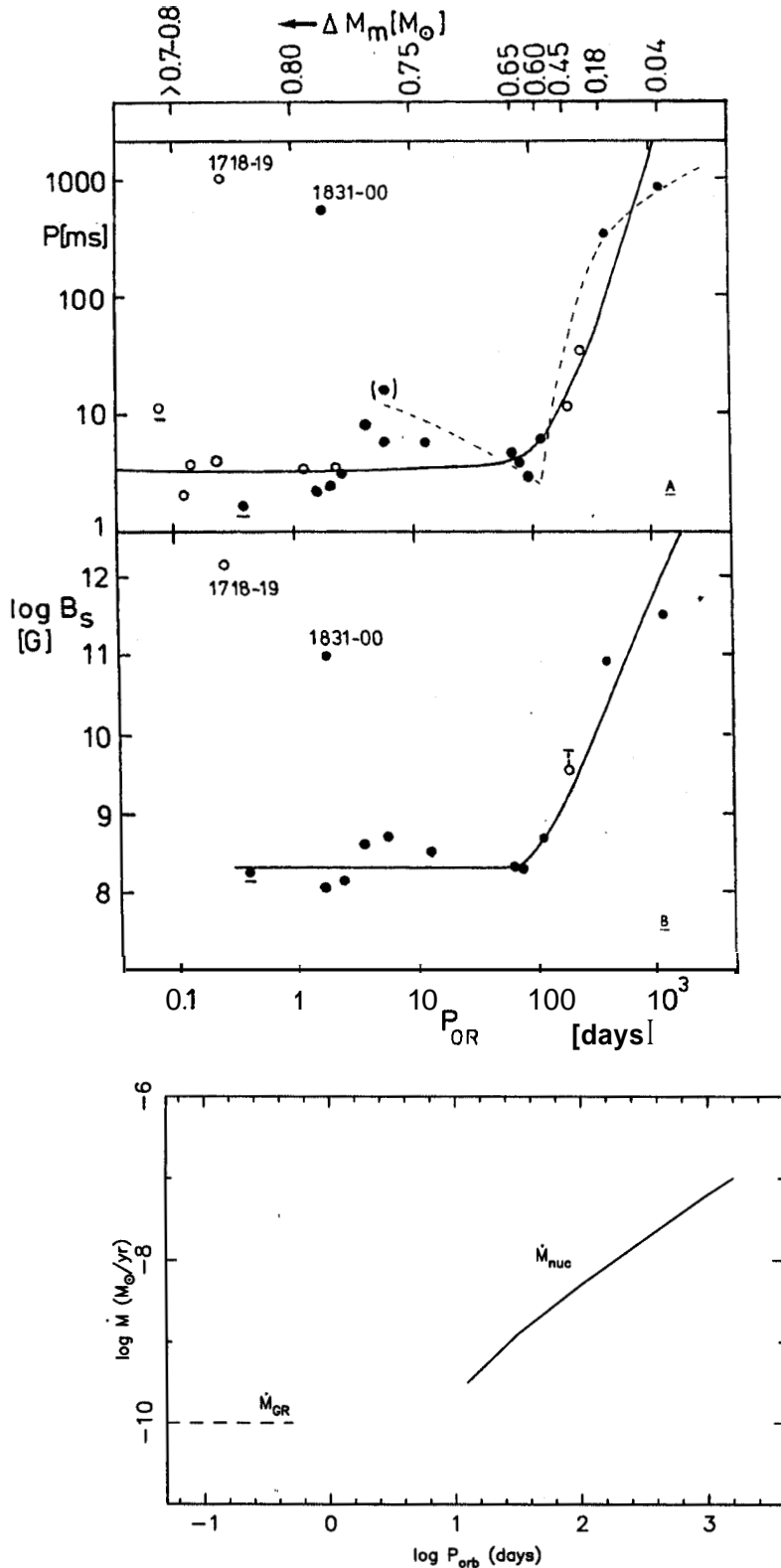


Figure 6.35: The top and the middle panels correspond to spin period, magnetic field vs. orbital period for binary pulsars with circular orbits and low-mass companions. The bottom panel depicts rate of mass transfer vs. the orbital period in low-mass X-ray binaries. \dot{M}_{GR} and \dot{M}_{nuc} correspond to mass transfers driven by gravitational radiation and by the nuclear evolution of the companion to the neutron star.

For longer periods the surface field increases with period. In the bottom panel the rate of accretion shows a similar increase with the orbital period. Therefore we see that for longer orbital periods higher rates of accretion and higher values of surface field are positively correlated. This is another observational indication that for higher rates of accretion the magnetic field strengths tend to be higher.

6.6 conclusions

In this chapter, we have looked at one of the model of magnetic field evolution assuming an initial crustal field configuration to check the consistency with the overall scenario of field evolution for isolated as well as binary pulsars. We find that the model can explain almost all the features that have been observed to date. And our conclusions can be summarized as follows :

- for this model to be consistent with the statistical analyses performed on the isolated pulsars at the most a maximum value of 0.05 for the impurity strength can be allowed;
- HMXBs produce high-field long period pulsars provided the duration of the wind accretion phase is short or the initial current distribution is located at higher densities;
- Relatively low-field ($B \sim 10^{10}$ Gauss) objects near death-line (low-luminosity pulsars) are also predicted from HMXBs;
- LMXBs will produce both high-field long period pulsars as well as low-field short period pulsars inclusive of millisecond pulsars in the later variety; and
- a positive correlation between the rate of accretion and the final field strength is indicated that is supported by observational evidence.